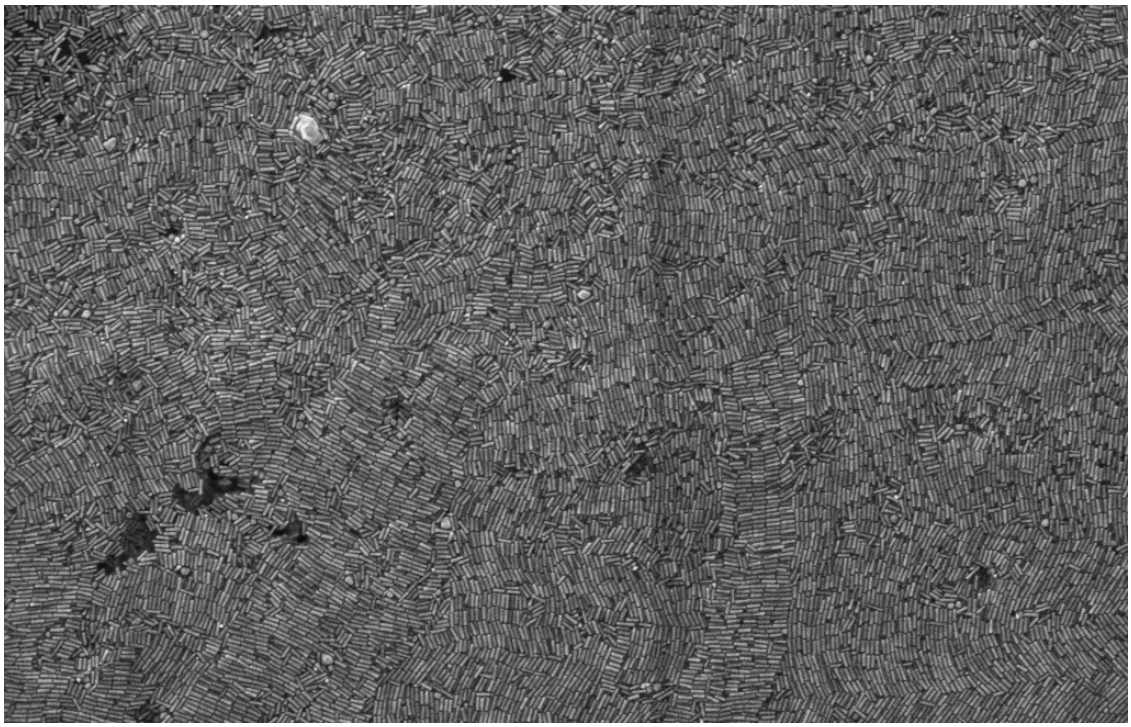

Synthesis of Gold Nanorods under the Influence of NIR Light

Master's thesis 2026

Mateo Galvis, Linda Strandberg

DEPARTMENT OF CHEMISTRY and CHEMICAL ENGINEERING

CHALMERS UNIVERSITY OF TECHNOLOGY
Gothenburg, Sweden 2026
www.chalmers.se

Master's thesis 2026

Synthesis of Gold Nanorods under the Influence of NIR Light

MATEO GALVIS, LINDA STRANDBERG

CHALMERS
UNIVERSITY OF TECHNOLOGY

Department of Chemistry and Chemical Engineering
Division of Applied chemistry
Martin Anderssons group
Chalmers University of Technology
Gothenburg, Sweden 2026

Synthesis of Gold Nanorods
under the Influence of NIR Light
MATEO GALVIS, LINDA STRANDBERG

Supervisor: Alida Ramdén, Applied Chemistry
Co-supervisor: Mats Hulander, Applied Chemistry
Examiner: Martin Andersson, Applied Chemistry

Master's Thesis 2026
Department of Chemistry and Chemical Engineering
Division of Applied Chemistry
Martin Andersson's group
Chalmers University of Technology
SE-412 96 Gothenburg
Telephone +46 31 772 1000

Cover: Scanning electron microscopy (SEM) image showing the morphology and ordered arrangement of synthesized gold nanorods (GNRs).

Typeset in LaTeX
Printed by Chalmers Reproservice
Gothenburg, Sweden 2026

MATEO GALVIS, LINDA STRANDBERG
Chemistry and Chemical Engineering
Applied Chemistry
Chalmers University of Technology

Abstract

Gold nanorods (GNRs) have attracted considerable attention due to their tunable optical properties and strong localized surface plasmon resonance (LSPR), making them relevant for applications in sensing, imaging, and photothermal therapy. Unlike spherical gold nanoparticles, GNRs have both transverse and longitudinal plasmon modes, where the longitudinal resonance strongly depends on particle aspect ratio. Precise control over nanorod growth is therefore essential for tailoring the optical response.

This thesis investigates how near-infrared (NIR) laser irradiation influences the seed-mediated synthesis of gold nanorods. Laser-irradiated samples were compared with non-irradiated controls prepared under identical conditions. Additional temperature-controlled experiments were conducted to distinguish the thermal effects from irradiation-related effects.

Characterization was performed using UV-Vis spectroscopy, scanning electron microscopy (SEM), and dynamic light scattering (DLS). UV-Vis analysis focused on longitudinal plasmon peak position, absorbance intensity, full width at half maximum (FWHM), rod index, and aspect ratio estimations. These observations were supported by SEM images analysed with ImageJ, which were used to evaluate morphology and aspect ratio distributions, while DLS measurements provided information on hydrodynamic diameter and colloidal stability.

The results show that laser irradiation affects both the synthesis process and the optical properties of the resulting nanorods. Laser-irradiated samples generally exhibited blue-shifted longitudinal plasmon peaks and reduced FWHM values compared to control samples, indicating lower aspect ratios and narrower particle distributions. This is supported by the SEM analysis, although aggregation and sampling limitations introduced uncertainty in the quantitative measurements. Lastly, DLS measurements were strongly affected by clustering and were therefore mainly used for qualitative evaluation.

In conclusion, NIR laser irradiation can influence GNRs growth during the synthesis and modify both morphology and optical properties.

Keywords: Gold nanorods, GNRs, seed-mediated synthesis, UV-Vis Spectroscopy, scanning electron microscopy, dynamic light scattering, localized surface plasmon resonance, nanomaterials, laser irradiation, aspect ratio.

Acknowledgements

We would like to thank everyone who supported us during this thesis.

First, we would like to thank our supervisor, Alida Ramdén, for her continuous support, positivity, and guidance throughout this project. You have always been approachable, welcoming, and encouraging, and have truly been important in helping us stay on track whenever we felt lost.

Secondly, we would also like to thank our co-supervisor, Mats Hulander, for always being available and willing to discuss our work. Your curiosity and engagement in our topic have been greatly appreciated, and your help with the lab equipment, especially when things were not working.

Thirdly, we would like to thank our examiner, Martin Andersson, for his insightful input and many new ideas. Together with our supervisors, you have created an open and supportive environment where it has always been easy to ask for help and discuss work.

We are especially grateful for the weekly Friday meetings with all three of you. These meetings have been highly appreciated and have played a significant role in keeping the project progressing. Being located on the same floor has also made communication easy and resulted in a collaborative atmosphere.

Additionally, we would also like to thank the people at the Division of Applied Chemistry, particularly those thesis workers and colleagues we have had the pleasure of sharing an office with during our time at the division. We would also like to thank John Andersson for his valuable help with the DLS equipment.

Finally, we would like to thank each other for cooperation, support, and teamwork throughout this thesis. Working together has been both rewarding and enjoyable, and we are grateful for the shared effort and encouragement along the way.

Mateo Galvis, Linda Strandberg, Gothenburg, May, 2026.

List of Abbreviations

Below is the list of acronyms that have been used throughout this thesis, listed in alphabetical order:

AA	L-ascorbic acid
$AgNO_3$	Silver nitrate
AR	Aspect ratio
BSE	Backscattered electrons
CTAB	Hexadecyltrimethylammonium bromide
FWHM	Full width at half maximum
GNP(s)	Gold nanoparticle(s)
GNR(s)	Gold nanorod(s)
$HAuCl_4$	Chloroauric acid
HCl	Hydrochloric acid
H_2O_2	Hydrogen peroxide
LSPR	Localised surface plasmon resonance
Milli-Q	Ultrapure water
$NaBH_4$	Sodium borohydride
NH_3	Ammonia solution
NIR	Near infrared
RPM	Revolutions per minutes
RI	Refractive index
SE	Secondary electrons
SEM	Scanning electron microscopy
TEM	Transmission electron microscopy
UV-Vis	Ultraviolet–visible spectroscopy

Nomenclature

Below is the nomenclature of symbols and parameters used throughout this thesis.

Sample Abbreviations

L	Laser-treated sample
CL	Control sample in the same water bath as the laser-treated sample
CW	Control sample in a separate water bath
L-WB	Laser water bath
C-WB	Control water bath

Sample Concentrations

Standard	Standard precursor concentration
E1	Elongated 1 precursor concentration
E2	Elongated 2 precursor concentration

Symbols

A	Absorbance
A_L	Absorbance at longitudinal peak
A_T	Absorbance at transverse peak
g	Gravitational acceleration (m/s^2)
c	Concentration (mol/dm^3)
D	Translational diffusion coefficient (m^2/s)
D_H	Hydrodynamic diameter (nm)
e	Elementary charge (C)

f	Pulse frequency (Hz)
h	Peak height
h	Planck's constant (Js)
I	Transmitted light intensity (cd)
I_0	Incident light intensity (cd)
k_B	Boltzmann constant (J/K)
l	Optical path length (cm)
m_e	Electron rest mass (kg)
T	Temperature (°C)
V	Accelerating voltage (kV)
$\Delta\lambda$	Peak shift (nm)
ε	Molar extinction coefficient (m^2/mol)
ε_m	Dielectric constant
η	Solvent viscosity (Pa·s)
λ	Wavelength (nm)
λ_L	Longitudinal plasmon peak wavelength (nm)
$\lambda_{\max}$	Longitudinal plasmon peak position (nm)
λ_T	Transverse plasmon peak wavelength (nm)

Contents

List of Figures

List of Tables

1

Introduction

Gold nanoparticles have been widely studied over the past two decades, due to their unique optical, electronic, and surface properties. Among various morphologies of nanoparticles, gold nanorods (GNRs) are interesting because of their anisotropic geometry, which results in a highly tunable localized surface plasmon resonance (LSPR) [1]. GNRs have also become attractive for biomedical applications, as they can tune near-infrared (NIR) light, penetrating biological tissue deeply while causing minimal damage [2]. Thus, the objective of this thesis is to analyse how NIR irradiation influences the synthesis and optical properties of GNRs.

When GNRs are illuminated at their LSPR wavelengths, absorbed photon energy is converted into heat through a non-radiative relaxation process. The optical properties of GNRs strongly depend on their size, morphology, and surrounding environment. Therefore, precise control of the GNR synthesis conditions is essential [3].

1.1 Nanoparticles and Gold Nanorods

Gold is generally considered biotolerant due to its low toxicity, making GNRs attractive for biomedical applications. During synthesis, GNRs are commonly stabilized with cetyltrimethylammonium bromide (CTAB). Since CTAB can be cytotoxic, it usually needs to be modified or replaced before biological use [4, 5].

1.2 Applications of Gold Nanorods

The unique optical and surface properties of GNRs have enabled their use in a wide range of biomedical applications, particularly in imaging, photothermal therapy, and targeted drug delivery [2, 3]. Their tunable LSPR, especially within the NIR region, allows efficient light absorption and photothermal conversion, making them suitable for minimally invasive therapeutic approaches [1, 3].

In photothermal therapy, GNRs can accumulate in tumor tissue and generate localized heat upon NIR irradiation, resulting in thermal ablation of cancer cells [3]. However, the influence of external NIR irradiation during nanorod growth is still not fully understood.

1.3 Aim of the Study

This thesis examines how NIR laser irradiation at different power levels influences the seed-mediated synthesis of GNRs. The study focuses on how laser exposure affects the growth, morphology, and optical properties of the synthesized nanorods, especially their aspect ratio (AR) and LSPR behaviour.

The influence of temperature and precursor concentrations, including ascorbic acid (AA) and silver nitrate ($AgNO_3$), as well as synthesis temperature, is evaluated in relation to the laser-assisted synthesis process. Irradiated samples are compared to non-irradiated control samples to study how laser irradiation affects GNR growth and optical behaviour during synthesis [1, 3, 5].

1.4 Scope and Limitations

Variations in precursor concentrations, including AA and $AgNO_3$, as well as synthesis temperature, are included in this study. The work is limited to GNRs and does not include other nanoparticle systems nor synthesis methods. Characterisation is performed using Ultraviolet-Visible Spectroscopy (UV-Vis), Dynamic Light Scattering (DLS), and Scanning Electron Microscopy (SEM).

2

Theory

This section introduces the theoretical foundations and relevant background for the research area of this thesis. This describes gold nanoparticles (GNPs) and their key properties, including their photothermal applications. This section also covers GNRs and their synthesis, surface plasmon resonance, and laser-assisted synthesis.

2.1 Gold Nanoparticles

GNPs have over the last few decades received growing interest in research because of their size-dependent properties. At the nanoscale (1-100nm), electron behaviour differs from that observed in bulk materials, leading to modified physical and chemical characteristics. These effects affect their optical and photothermal response, which has been used in applications such as biosensing, diagnostic imaging, and targeted cancer therapy. Since these properties are sensitive to particle size and morphology, reliable control of nanoparticle growth is important [6, 7].

2.2 Gold Nanorods

GNRs are rod-shaped gold nanoparticles that have tunable plasmonic properties, which are not observed in larger bulk nor in spherical nanoparticles. Unlike other GNPs, GNRs exhibit two types of resonant modes, as illustrated in figure 2.1. It has a transverse mode where electrons oscillate perpendicular to the long axis, and a longitudinal mode corresponding to oscillation along the long axis [8].

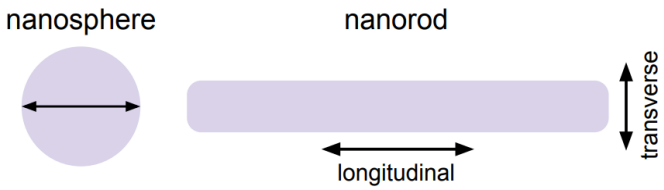

Figure 2.1: Comparison of LSPR modes in nanospheres and nanorods: Spheres exhibit a single plasmon mode, whereas nanorods exhibit both transverse and longitudinal oscillations.

GNRs are chemically stable and have a large surface area to volume ratio. In addition, their surfaces can be functionalized with ligands, polymers, and proteins [9, 10].

2.2.1 Seed-Mediated Growth of Nanorods

GNRs are synthesized using a seed-mediated growth method, where small GNPs act as nucleation sites for continued growth steps. Gold ions are reduced onto these seeds during controlled synthesis conditions, leading to anisotropic growth [1].

A mild reducing agent controls the reduction rate, while surfactants and silver ions influence the growth direction by stabilizing specific crystal facets. This suppresses lateral growth and promotes elongation along the longitudinal axis [1].

The AR of the nanorods can be adjusted by varying precursor concentrations, reaction conditions, and the presence of silver ions, which influence the optical properties and longitudinal plasmon resonance of the GNRs [1]. Therefore, precise control of the synthesis parameter is essential for obtaining nanorods with specific dimensions and optical behaviour.

2.2.2 Factors Affecting Aspect Ratio (AA, $AgNO_3$)

The AR of GNRs is influenced by the concentrations of AA and $AgNO_3$. AA acts as a mild reducing agent by reducing Au^{3+} ions to Au^{1+}, which controls the reduction rate and affects the growth kinetics of the GNR [1].

Silver ions selectively adsorb onto specific crystal facets, suppressing lateral growth while promoting elongation along the longitudinal axis. As a result, variations in the concentrations of AA and $AgNO_3$, the growth kinetics, and relative facet stabilization can be controlled, which directly affect the AR of the resulting GNR [1].

2.3 Optical Properties and UV-vis Spectroscopy

UV-Vis spectroscopy is used to measure the absorbance of light at different wavelengths and to give information about the optical properties of nanoparticles. By observing the absorbance over a range of wavelengths, an absorption spectrum is obtained [11].

For GNPs and GNRs, the optical response comes from interactions between the incident light and conduction electrons, resulting in characteristic absorption peaks in the UV-Vis region [11].

2.3.1 Beer-Lambert Law

The absorbance A is defined as the logarithmic ratio between the incident and transmitted light intensity, shown in Equation 2.2:

$$A = -log_{10}(\frac{I}{I_0}) \tag{2.1}$$

where I_0 is the incident light intensity, and I is the transmitted intensity. For dilute systems, the absorbance is related to the concentration according to the Beer-Lambert law in Equation 2.2 [12]:

$$A = \varepsilon c l \tag{2.2}$$

where ε is the molar extinction coefficient, c is the concentration, and l is the optical path length. This relationship is used in UV-Vis spectroscopy, where absorbance is measured as a function of wavelength to obtain an absorption spectrum [11].

In the case of GNPs and GNRs, the absorption spectra are dominated by LSPR, which produces characteristic peaks in the UV-Vis region [1].

2.3.2 Localized Surface Plasmon Resonance

GNPs LSPR is when incident electromagnetic radiation induces collective oscillations of conduction electrons at the nanoparticle surface. This collective electron oscillation is illustrated in figure 2.2. The excited electrons can relax through radiative scattering or a non-radiative relaxation process that converts absorbed energy into heat [13].

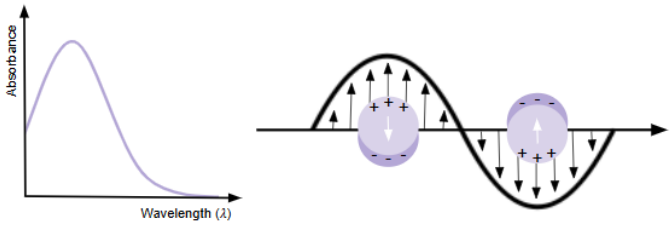

Figure 2.2: Schematic illustration of LSPR for GNPs. The figure shows how incident light induces collective oscillations of free electrons at the GNP surface and the resulting absorption behaviour.

The morphology of GNPs also significantly influences their plasmonic resonance mode. Spherical nanoparticles typically exhibit a single plasmon resonance mode, while anisotropic nanoparticles such as GNRs display both transverse and longitudinal resonance modes due to their elongated geometry. The longitudinal mode is highly dependent on the AR of the GNRs and can therefore be tuned into the NIR region [7, 9].

The wavelength at which LSPR occurs depends on several characteristics of the GNPs. In particular, the electron density at the particle surface is important and is influenced by factors such as particle size, shape, and the dielectric properties of both the GNPs and the surrounding medium. Another important parameter is the refractive index (RI) of the surrounding medium. RI describes how light propagates through a medium relative to its speed in a vacuum. Thereby, variations in the refractive index of the surrounding medium can cause shifts in the LSPR frequency. This can be studied by looking at an absorption spectrum [1].

2.3.3 Ultraviolet-Visible Spectroscopy

UV-Vis spectroscopy is commonly used to analyse absorption spectra to quantify compounds in solution. For GNRs, the position and shape of the absorption peaks provide information about particle [11].

2.3.4 Aspect Ratio and Peak Position

The transverse and longitudinal plasmon resonance modes of GNRs are illustrated in figure 2.3. The longitudinal mode is strongly influenced by the geometry and AR of the nanorods.

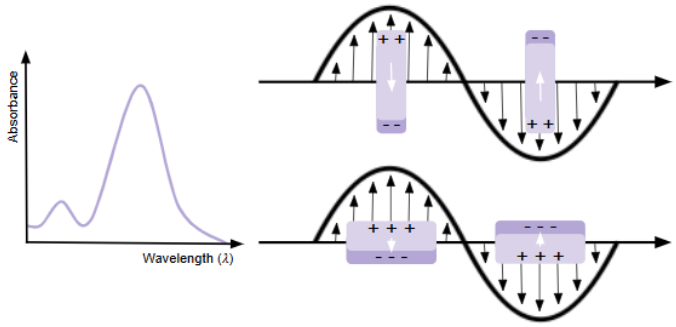

Figure 2.3: Illustration of LSPR in a GNP. Incident light induces oscillations of surface electrons along the electric field, resulting in an absorption peak. In anisotropic nanoparticles, oscillation can occur along different axes, giving rise to transverse and longitudinal modes that result in two absorption peaks.

AR is the ratio between the length and the width of a nanorod, defined in Equation 2.3. AR dependence becomes particularly important during the growth synthesis. The LSPR can be tuned into the NIR region, allowing NIR irradiation to interact with the plasmon resonance of the GNRs. NIR irradiation is therefore justified by the optical properties predicted by Gans Theory [14].

$$AR = \frac{length}{width} \tag{2.3}$$

This relationship is central for interpreting UV-Vis spectra of GNRs and enables estimation of the AR from the position of the longitudinal peak. It also provides a physical basis for the use of NIR irradiation, as the excitation wavelength can be matched to the LSPR of the particles [15].

The plasmon resonance is strongly dependent on the geometry of the nanorods. As the AR increases, the longitudinal resonance shifts to longer wavelengths, which is observed as a shift in the absorption peak ($\Delta\lambda$), illustrated in figure 2.4 [14, 1].

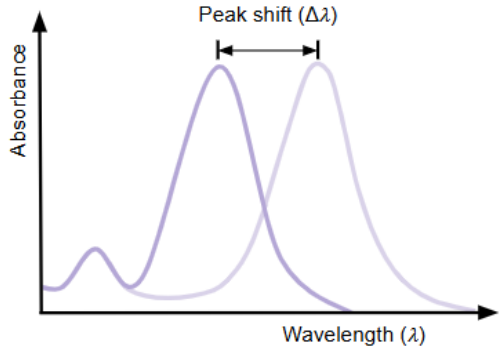

Figure 2.4: Illustration of peak shift ($\Delta\lambda$) in UV-Vis spectra.

The displacement of the absorption maximum reflects changes in the optical properties of the nanoparticles. A shift towards longer wavelengths (red-shift) indicates an increase in AR, while a shift towards shorter wavelengths(blue-shift) indicates a decrease.

2.3.5 Rod-Index

The ratio between the absorption of the longitudinal and transverse peaks is referred to as the ROD-index, shown in Equation 2.4.

$$\text{ROD-Index} = \frac{A_{Longitudinal}}{A_{Transverse}} \tag{2.4}$$

A higher ROD-index generally indicates a greater contribution of rod-shaped nanoparticles and is evaluated as nanorod purity and yield [16].

2.3.6 Peak Width and Size Distribution

The width of the longitudinal peak in a UV-Vis spectrum can be used as an indicator of the distribution of particle properties within a sample. A broader peak indicates a wider distribution, while a narrower peak indicates a more uniform population in the absorption range that is directly connected to the GNRs size. One way to compare the distributions is to calculate full width at half maximum (FWHM), as illustrated in figure 2.5 [15].

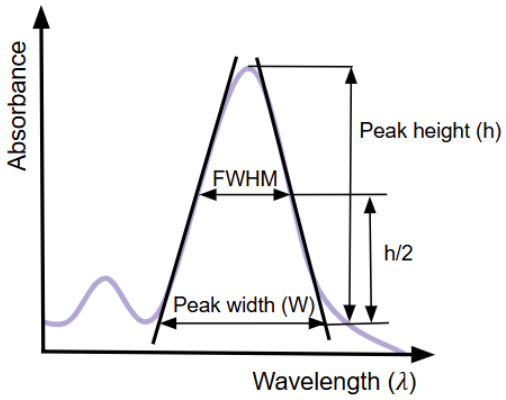

Figure 2.5: Schematic illustration of peak width determination in a UV-Vis spectrum. The peak height (h) is defined relative to the local minimum adjacent to the peak, and half of this height ($h/2$) is used as a reference level. The width of the peak at a height of $h/2$ is denoted FWHM.

2.4 Dynamic Light Scattering

DLS is used to determine the size distribution of nanoparticles in suspension. The technique is based on fluctuations in the intensity of scattered light caused by the Brownian motion of particles in a liquid. Smaller particles diffuse faster than larger ones, which results in more rapid fluctuations in the detected signal [17].

The intensity fluctuations are analysed with an autocorrelation function, from which the translational diffusion coefficient, D, is obtained. This coefficient is related to the hydrodynamic diameter, D_H, through the Stokes-Einstein Equation 2.5:

$$D = \frac{k_B T}{6\pi\eta D_h} \tag{2.5}$$

where k_B is the Boltzmann constant, T is the absolute temperature, and η is the viscosity of the solvent. The D_H corresponds to the radius of a sphere that diffuses at the same rate as the particle, therefore it includes contributions from any surface-bound species or solvation layers [17].

Since DLS assumes spherical particles, the method does not directly describe anisotropic systems such as GNRs. Instead, the reported D_H should be used as an effective value reflecting the overall diffusion behaviour. For nanorods, this value depends on both length and diameter, as well as their orientation in solution. Therefore, an increase in AR leads to slower diffusion, which should result in a larger measured D_H [17].

2.5 Scanning Electron Microscopy

SEM is a type of electron microscope that produces high-resolution images using a focused beam of electrons to scan the surface. SEM relies on the principle of the de

Broglie relation; electrons that are accelerated between 3-30 kV possess a wavelength several times smaller than light, enabling superior spatial resolution. SEM is based on de Broglie wavelength (λ) shown in Equation 2.6 [18].

$$\lambda = \frac{h}{\sqrt{2m_e eV\left(1 + \frac{eV}{2m_e c^2}\right)}} \tag{2.6}$$

Where λ denotes the electron wavelength, h is Planck's constant, m_e is the rest mass of the electron, e is the elementary charge, V is the applied accelerating voltage, and c is the speed of light in vacuum. The relativistic correction term $\left(1 + \frac{eV}{2m_e c^2}\right)$ becomes significant at high accelerating voltages [18].

Primary electrons have high energy that penetrates the surface of the sample and generates an interaction volume. This interaction produces different types of signals, the most important of which are secondary electrons (SE), and backscattered electrons (BSE). SE are low-energy electrons that are ejected from the near-surface (<10 nm), they are highly sensitive and are used in conventional SEM images. BSE are high-energy electrons that are ejected from deeper parts of the sample. Their yield is correlated to the samples atomic number, giving composition contrast, where heavier elements appear lighter colours [18].

SEM samples are analysed in vacuum to prevent any scattering from the gas molecules or contaminations of the beam. Non-destructive samples must be conductive or coated with a thin layer of conductive material (e.g gold or platinum) to dissipate the charge build-up caused by the incident electron beam, which would otherwise distort the image [18].

3

Methods

This section outlines the methods and materials used in the experiments performed in this study. This section provides an overview of the materials and equipment used during the GNR synthesis and the experimental procedure, setup, purification, and characterisation methods.

3.1 Materials

The chemicals used in this work included hexadecyltrimethylammonium bromide (CTAB), chloroauric acid ($HAuCl_4$), silver nitrate ($AgNO_3$), L-ascorbic acid (AA), sodium borohydride ($NaBH_4$), and hydrochloric acid (HCl, 37%), which were applied in the synthesis of GNRs. All chemicals were purchased from Sigma-Aldrich.

Ultrapure water (Milli-Q, 18.2 MΩ·cm) was used for all solution preparation. Solutions were prepared at concentrations stated under section 3.2. UV-Vis absorption measurements were performed with using a spectrophotometer (Thermo Fisher Scientific Oy, Multiskan GO). After synthesis, the samples were centrifuged (Thermo Scientific, MegaFuge 16R) to remove excess reactants. The supernatant was discarded and the particles were redispersed in Milli-Q water.

Following the synthesis, the samples were analyzed using SEM (Carl Zeiss AG, Zeiss Ultra 55) and DLS (Litesizer 500, Anton Paar)

All glassware was cleaned using a basic piranha solution composed of Milli-Q water, ammonia solution (NH_3, 28%), and hydrogen peroxide (H_2O_2) in a 5:1:1 ratio. After cleaning, all items were thoroughly rinsed with Milli-Q water and dried with nitrogen gas.

Laser irradiation experiments were conducted using a NIR diode laser (BWT Beijing DS3-51523, K808FA5FN-50.00W, $\lambda \approx 808$ nm). The laser beam was expanded using a collimator and a beam expander (Thorlabs GBE02-B, 2×). The laser settings used during the NIR irradiation experiments are summarized in Table 3.1.

Table 3.1: Laser settings used during NIR irradiation experiments.

Parameter	Setting
Wavelength	808 nm
Temperature setpoint	25 °C
Frequency setpoint	10000 Hz
Pulse width	95 μs
Operation mode	Continous wave

Water baths were used to maintain controlled temperature conditions throughout all experiments. Temperature monitoring during the experiments was performed using an infrared thermal camera (Testo 871s).

3.2 Synthesis of Gold Nanorods

GNRs were synthesized using a seed-mediated growth approach using a CTAB-based system. All synthesis steps were carried out in a water bath maintained at 30 °C.

3.2.1 Seed Synthesis (SEEDS@CTAB)

The seed solution was prepared by adding 4.7 mL of CTAB (0.1 M) to a reaction vial, followed by 25 μL of $HAuCl_4$ (50mM). The mixture was stirred at 400 RPM until the solution appeared uniform and no visible particles remained.

A freshly prepared $NaBH_4$ solution (10mM, 300μL) was quickly added while increasing the stirring speed to 1400 RPM for approximately 10-20 seconds. This step resulted in a light brown solution, indicating the formation of seeds. The stirring speed was then reduced to 400 RPM, and the solution was kept at 30 °C.

3.2.2 Growth of Single-GNRs Without NIR Irradiation

For the growth solution, 10 mL of CTAB (0.1 M) was added to an Erlenmeyer flask. Then, 100 μL of $HAuCl_4$ (50 mM) and 190 μL of HCl (1 M) were introduced. The solution was placed in the water bath and gently stirred for 5 minutes or until homogeneous.

Before continuing, the magnetic stir bar was removed from the flask. Then 120 μL of $AgNO_3$ (10 mM) was added, and the flask was gently mixed by hand. After this, 100 μL of AA (100 mM) was added, causing the solution to become colourless within a few seconds.

Finally, 24 μL of the seed solution was added, and the mixture was briefly mixed to initiate GNR growth. Depending on the experiment, the solution was either left in

the original Erlenmeyer flask or distributed into multiple containers. The samples were then left undisturbed in the water bath for two hours.

3.2.2.1 Modified Concentrations for Elongated Nanorods

For experiments targeting longer GNRs, the concentration of AA and $AgNO_3$ was adjusted while all other synthesis parameters remained constant. The precursor concentration used for synthesis of elongated GNRs is summarized in Table 3.2.

Table 3.2: Precursor concentrations used for synthesis of gold nanorods.

Sample	AA (mM)	$AgNO_3$ (mM)
Standard	100	10
Elongated 1	90	11
Elongated 2	80	12

3.2.3 Experimental Setup for NIR Irradiation

Following the synthesis, the GNR solution was divided into three separate samples. Two samples were placed in the same water bath with a magnetic stirrer shown in Figure 3.1a, where one sample was exposed to NIR laser irradiation while the other served as a control. To minimize unintended exposure, a physical barrier made of aluminium was placed between the samples. In addition, the third control sample was prepared and placed in a separate water bath in a different fume hood, illustrated in Figure 3.1b, and used as a reference to exclude any influence from scattered light or laser-induced heating.

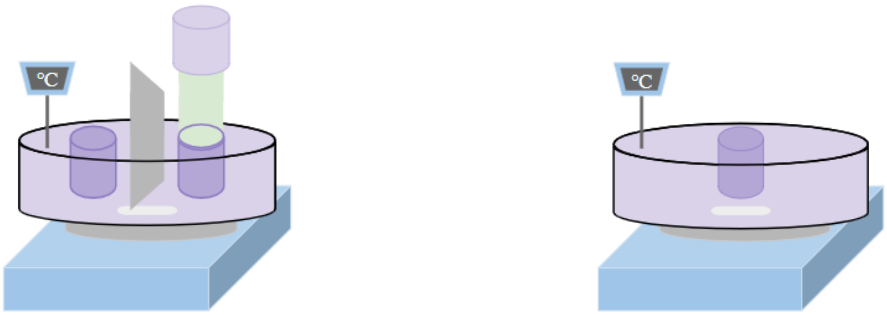

(a) **(b)**

Figure 3.1: (a) Schematic illustration of the laser-assisted synthesis setup. Samples were placed in temperature-controlled water baths with magnetic stirring, and temperature was monitored using a probe connected to the hot plate. (b) An identical sample was placed in a separate water bath in a different fume hood, without laser irradiation.

Both flat-bottomed crystallizing dishes were placed on a temperature-controlled hotplate. To minimize evaporation in all samples without hindering the NIR light in the exposed sample, thin glass plates were placed over the openings.

3.2.4 Experimental Setup for Temperature Synthesis

To understand the impact temperature has on the synthesis, the original synthesis was divided into four identical samples. Each sample was placed in a separate water bath set at 30, 35, 40, and 45 °C. The temperature in each water bath was controlled using a heating element. The setup is illustrated in Figure 3.2.

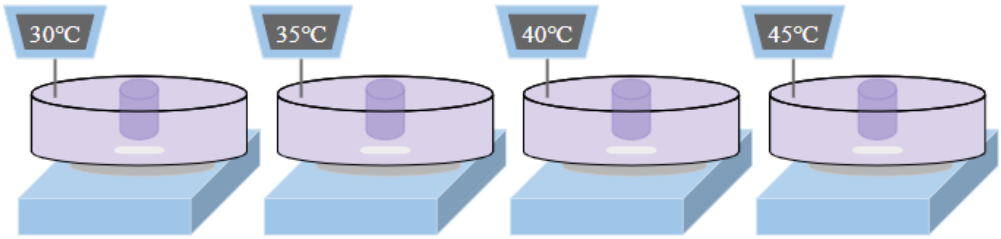

Figure 3.2: Illustration of the experimental setup used to study the effect of temperature on the nanorod synthesis. The growth solution was divided into four identical samples and placed in separate water baths at 30, 35, 40, and 45 °C.

Precisely as in an ordinary synthesis, the sample is placed into a flat-bottomed crystallizing dish together with a magnet stirrer. During the entire synthesis, a glass lid was placed on the samples to minimize evaporation.

3.2.4.1 Measurements During Synthesis

Measurements during GNR synthesis were made at different time points throughout the experiment. UV-Vis spectra were recorded continuously to monitor nanoparticle formation and growth. In addition, the temperature of the water bath and the probe was monitored using a thermal camera.

3.2.5 Purification

Three consecutive centrifugation steps were performed to purify the synthesised GNRs with the settings displayed in Table 3.3 at approximately 30°C.

Table 3.3: Centrifugation steps for purification of synthesised gold nanorod.

Step	Centrifugation	Time	Sample Composition
1	1900 $\times g$	30 min	Whole nanorod solution
2	1800 $\times g$	30 min	0.5 mL pellet + 3.5 mL Milli-Q water
3	1800 $\times g$	30 min	333 μL pellet + 3.66 mL Milli-Q water

Following the third centrifugation step, 100 μL of pellets were diluted in 733 μL of Milli-Q water in safe-lock microcentrifuge tubes. All tubes were covered with aluminium foil to protect them from light and placed in the fridge for preservation.

3.3 Characterization of GNRs

The synthesized GNRs were characterized using UV-Vis, SEM, and DLS.

3.3.1 UV-Vis Spectroscopy and LSPR Analysis

The optical properties of GNRs were characterised using UV-Vis spectroscopy. Absorbance spectra were recorded in a wavelength range of 400-1000 nm. Before measurement, samples were diluted 1:100 in Milli-Q water. All measurements were performed in microcuvettes with a path length of 1 cm, using Milli-Q water as the blank reference. The AR was estimated from the longitudinal plasmon peak position from the UV-Vis spectra using the relation shown in Equation 3.1:

$$AR = 0.79 + \frac{\lambda_{\max} - 495.14}{53.71\,\varepsilon_m} \tag{3.1}$$

where λ is the maximum wavelength and $\varepsilon_m = 1.77$ is the dielectric constant of water [19]. In addition, FWHM was calculated from UV-Vis to determine the polydispersity of the GNRs. The spectra were monitored during different time intervals to assess sample quality.

3.3.2 Scanning Electron Microscopy (SEM)

The morphology of the synthesised GNRs was characterised using SEM. The samples were prepared by diluting the pellets obtained after purification in a 1:200 ratio using Milli-Q water. 20 μL of the diluted sample was deposited on a clean silicon wafer substrate that was mounted on a SEM-stub using conductive carbon tape. The sample was allowed to evaporate at room temperature before imaging. All images were characterized using the SE mode with an acceleration voltage between 2-3 kV.

The silica wafers were prepared in an Ultrasonic Cleaning procedure as summarized in Table 3.4.

Table 3.4: Ultrasonic cleaning steps

Step	Solvent	Time	Power
1	Acetone	5 min	3
2	Ethanol	5 min	3

After each sonication step, the wafer was rinsed thoroughly with Milli-Q water to remove residual solvent. The wafers were then dried under a stream of nitrogen gas.

To further remove organic contaminants and improve surface cleanliness, the wafers were treated in a UV-ozone cleaner for 15-20 minutes.

3.3.2.1 ImageJ

ImageJ is an image processing program that was used to calculate the AR of the GNRs. The measurement for calculating AR was done by fitting the rods as ellipses in order to obtain the length and width of the selected image. The selected GNRs were obtained by using threshold input and manually erasing the spheres or attached particles. The same method was applied to all selected GNRs, with the pixel/nm scale adjusted accordingly to ensure accurate determination of the AR.

3.3.3 Dynamic Light Scattering (DLS)

DLS measurements were preformed at 25 °C. The synthesised GNRs samples were diluted at different concentrations (1:100, 1:150, 1:200, 1:250) in Milli-Q water and loaded into disposable cuvettes (*Eppendorf Se, Germany*). Each measurement consisted of 6 rounds, each one being 6 seconds long. The autocorrelation functions were used to obtain the average hydrodynamic diameter and polydispersity index (PDI).

3.3.4 AI as a tool

Generative AI tools, such as Claude (Opus4.7) and ChatGPT (OpenAI), were used in this study as writing and formatting aids. Their use was limited to paragraph structuring, citations, and grammatical guidance. It provided help on coding diagrams and plots in MATLAB, but also on formatting Figures and Tables in LaTeX. All scientific content, experimental work, data analysis, and interpretations were carried out by the authors, even the Illustrations in the Theory chapter.

4

Results

Variations in laser power, synthesis temperature, and precursor composition resulted in measurable differences in the optical properties of the synthesized gold nanorods. To evaluate these effects, the samples were characterized using UV-Vis spectroscopy, SEM, and DLS. The characterisation results are presented in the following sections.

4.1 UV–Vis Results

UV-Vis spectroscopy was used to evaluate how the synthesis conditions affected the optical response of the GNRs. The results are presented first by validating the control condition, followed by comparisons of final spectra, time-resolved spectral development, temperature-dependent controls, modified synthesis conditions, and peak width analysis.

4.1.1 Validation of the Control Conditions

For validation of the control conditions, representative UV-Vis spectra of the control samples and the laser-exposed samples are presented in Figure 4.1.

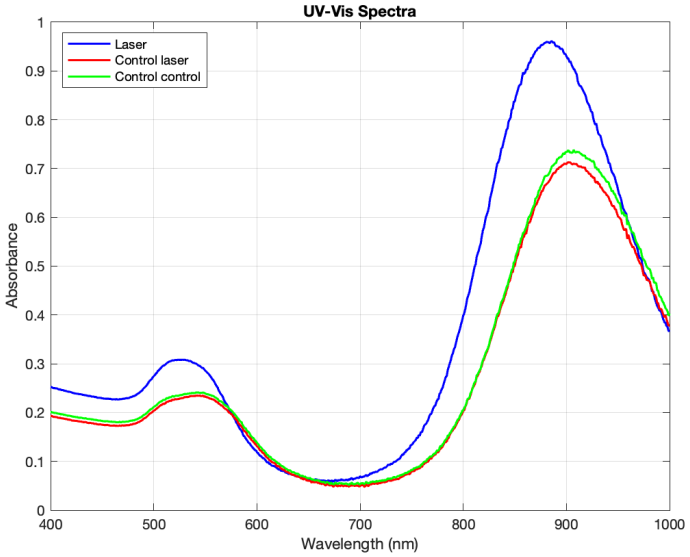

Figure 4.1: Representative UV-Vis spectra for the laser-exposed sample and the two control samples used for validation of the control conditions.

As shown in Figure 4.1, the two control conditions displayed similar spectral profiles overall. The positions of both the longitudinal and transverse plasmon bands were comparable. Additional measurements are provided in Table A.1 in Appendix A, where the peak positions at different laser powers are summarized. To compare the samples further, the transverse and longitudinal plasmon bands were evaluated separately.

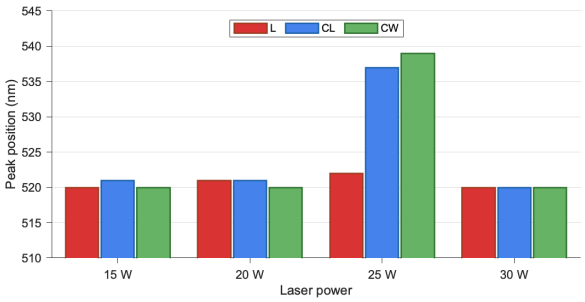

Figure 4.2: Transverse plasmon band, comparing laser and two control groups at different power effects.

Figure 4.2 shows that the CL and CW samples remained similar at all laser powers. Although a larger difference between the control conditions and the laser-irradiated sample appeared at 25 W.

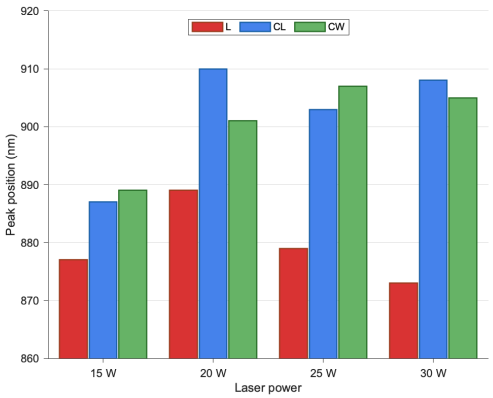

Figure 4.3: Longitudinal plasmon band, comparing laser and two control groups at different power effects.

In Figure 4.3, the same overall pattern can be seen. The CL and CW samples stayed close to each other, while the laser-treated samples consistently showed lower values.

Since the control sample placed in the same water bath as the laser-treated sample showed similar UV-Vis spectra to the control in a separate bath, the CL condition was used as the main control in the following analysis.

4.1.2 Longitudinal Plasmon Peak Shift

The difference in the longitudinal plasmon peak between CL and L samples was calculated to quantify the spectral shift induced by laser irradiation. The wavelength difference ($\Delta\lambda_L$) was defined as Equation 4.1 states:

$$\Delta\lambda_L = \lambda_{L,\mathrm{CL}} - \lambda_{L,\mathrm{L}} \tag{4.1}$$

where $\lambda_{L,\mathrm{CL}}$ corresponds to the longitudinal plasmon peak position of the CL sample and $\lambda_{L,\mathrm{L}}$ corresponds to the longitudinal plasmon peak position of the L sample.

Table 4.1: Longitudinal plasmon peak differences between CL and L samples

Power (W)	$\Delta\lambda_L$ **(nm)**
15	10
20	21
25	24
30	35

As shown in Table 4.1, all L samples exhibited a smaller longitudinal plasmon peak position compared to their CL samples. The peak shift size increased with laser power, with the largest shift observed for the 30 W sample.

4.1.3 Time-Resolved Spectral Development

Time-resolved UV-Vis measurements were performed to evaluate the spectral development during synthesis. A representative experiment was selected to compare the temporal evolution of L and CL.

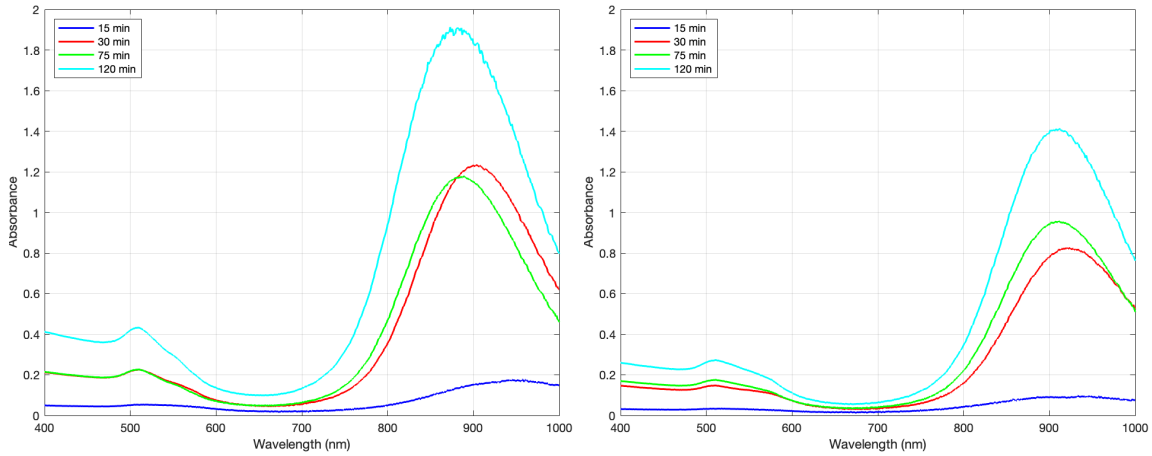

(a) **(b)**

Figure 4.4: (a) 30 W L synthesis for Standard precursor concentrations (b) the corresponding CL synthesis.

As shown in Figure 4.4a, the L sample exhibits a rapid shift in the longitudinal plasmon peak during the initial stages of synthesis, with most of the spectral change occurring faster than the CL samples.

The difference in time-resolved spectral development is further illustrated in Figure 4.5, where the longitudinal peak position is plotted as a function of time. The laser-exposed sample reached a near-final peak position significantly earlier than the control sample.

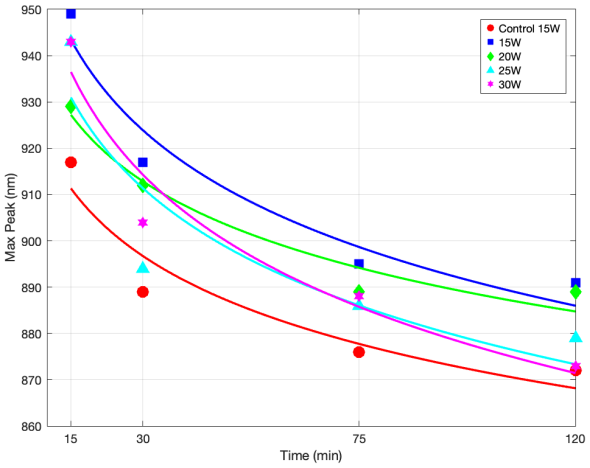

Figure 4.5: Power regression analysis of the longitudinal peak maximum during L synthesis at different laser powers together with the representative CL at 15 W.

Among the evaluated regression models, the power regression produced the highest goodness-of-fit (R^2) values. Increasing laser power resulted in more negative regression exponents, indicating faster temporal reductions in longitudinal peak wavelength at higher intensities. The calculated functions are shown in Figure 4.5 and the corresponding R^2 values are presented in Table 4.2.

Table 4.2: Power regression analysis of λ_{max} as a function of time for L samples and the representative CL at 15 W.

Sample	Reggression	b-value	R^2
Laser 15 W	$y = 971x^{-0.0233}$	-0.0233	0.912
Laser 20 W	$y = 986x^{-0.0225}$	-0.0225	0.956
Laser 25 W	$y = 1012x^{-0.0307}$	-0.0307	0.810
Laser 30 W	$y = 1028x^{-0.0346}$	-0.0346	0.944
Control 15 W	$y = 1024x^{-0.0302}$	-0.0302	0.945

Power regression analysis showed temporal decreases in longitudinal peak position across all samples. Higher laser power generally produced more negative regression exponents, indicating faster peak shifts. The most negative exponent occurred at 30 W ($b = -0.0346$), with 15 W and 20 W showing progressively less negative values, confirming a trend of increasingly negative b-values with increasing laser power.

4.1.4 Temperature Monitoring During Synthesis

A representative thermal image of the experimental setup is shown in Figure 4.6.

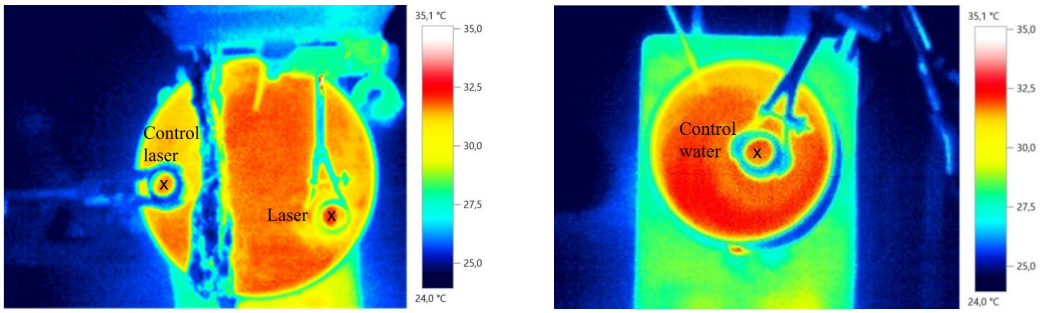

(a) **(b)**

Figure 4.6: Representative thermal images of the experimental setups. (a) Thermal image of L and CL in the same waterbath. (b) Thermal image of control synthesis in an identical waterbath (separate fume hood).

Following the representative thermal images shown in Figure 4.6, the temperature evolution during GNR synthesis at different laser powers is presented in Figure 4.7.

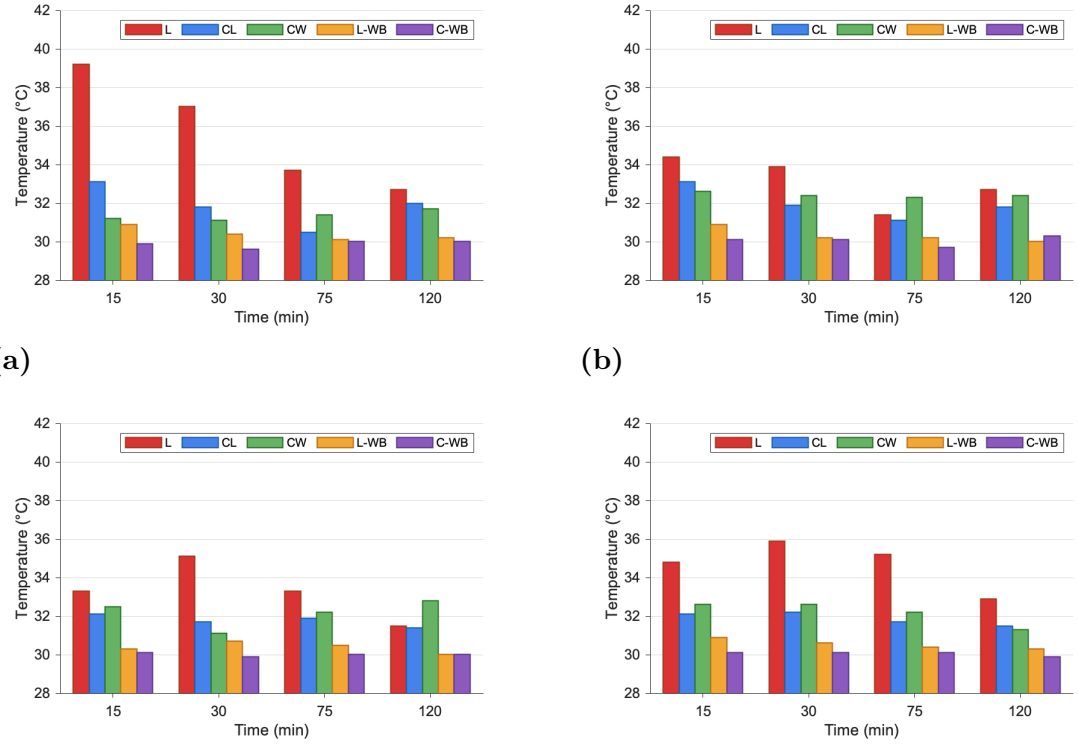

(a) **(b)**

(c) **(d)**

Figure 4.7: Temperature measurements during GNR synthesis at different laser powers: (a) 15 W, (b) 20 W, (c) 25 W, and (d) 30 W. Temperatures of the two waterbaths, laser water bath (L-WB) and control water bath (C-WB), were also recorded at different times.

Higher temperatures were measured for L samples compared to both CL and CW synthesis at all investigated powers. The measured temperatures presented in Figure 4.7 are stated in Table A.2, in Appendix A. The largest temperature differences between L and CL were observed during the initial stages of the synthesis, after which the temperatures gradually decreased over time. Additionally, more condensation was observed on the glass walls of the L compared to CL. A representative image of the setup after the experiment is shown in Figure 4.8.

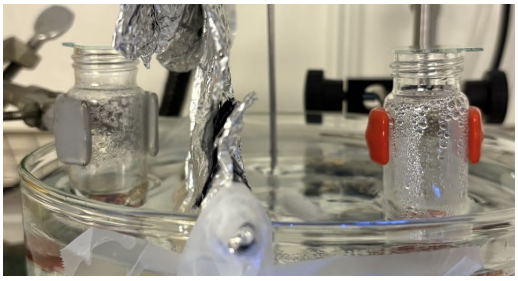

Figure 4.8: Setup during a synthesis, showing that the (left) L sample has more condensation on its glass walls, compared to the (right) CL sample.

4.1.5 Temperature-Dependent Control Experiments

To distinguish thermal effects from other possible effects of laser irradiation, temperature-dependent control experiments were performed without laser exposure. Representative UV-Vis spectra recorded after 30, 75, and 120 min for each temperature are presented in Figure A.1, in Appendix A, while the extracted longitudinal plasmon peak positions are summarized in Figures 4.9 and 4.10.

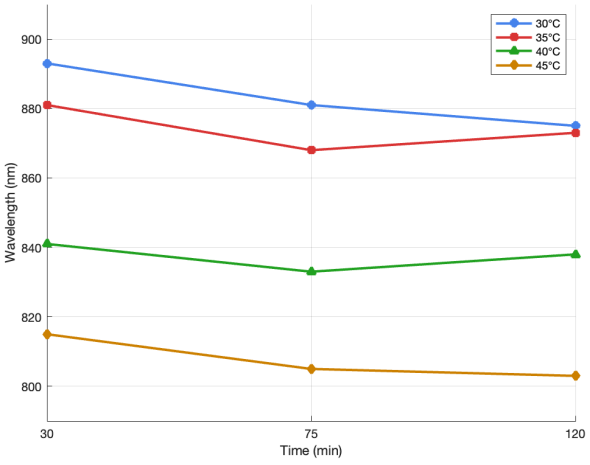

Figure 4.9: λ_{max} obtained from UV-Vis measurements after 30, 75, and 120 minutes at 30 °C, 35 °C, 40 °C, and 45 °C.

At the intermediate temperatures, λ_{max} approached its final position within a shorter time interval, whereas the lowest and highest temperatures displayed a more gradual evolution.

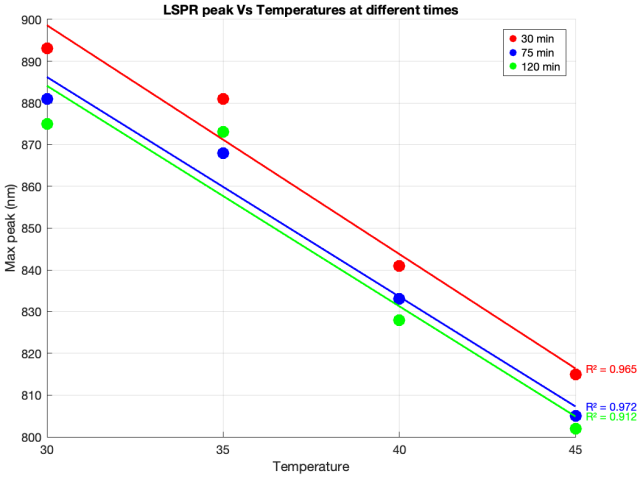

Figure 4.10: λ_{max} as a function of synthesis temperature at different reaction times (30, 75, and 120 min).

Increasing synthesis temperature was associated with a shift of the longitudinal plasmon peak towards longer wavelengths at all investigated time points. A similar trend was observed for all reaction times, indicating a consistent influence of temperature on both the temporal spectral evolution and the final λ_{max} throughout the synthesis.

4.1.6 Effect of Modified Precursor Concentrations

UV-Vis spectra were recorded for L and CL samples at modified precursor concentrations. Samples for 25 W and 30 W are found in Figure A.2, in Appendix A.

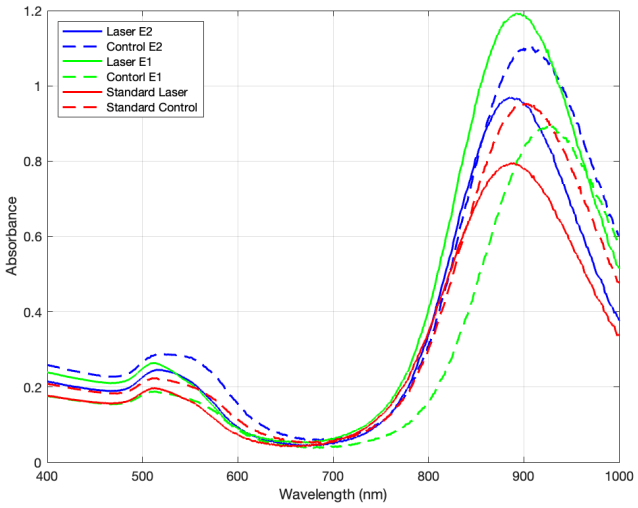

Figure 4.11: UV-Vis spectra of GNRs synthesised at different concentrations represented in E1, E2, and standard conditions. For both laser irradiated at 20 W.

Figure 4.11 illustrates that both the L and the CL group at different concentrations were successfully synthesised as both transverse and longitudinal plasmon resonance peaks are seen. The E1 sample with the precursor concentrations shown in Table 3.2 exhibits the highest longitudinal absorbance ($\sim$ 1.19), reflecting a higher yield of GNRs.

The λ_{max} position for L and CL synthesized at different laser powers and precursor concentrations is summarized in Table 4.3.

Table 4.3: Longitudinal plasmon peak positions for L and CL control samples.

	Standard			**Elongated 1**			**Elongated 2**		
Power (W)	**L**	**CL**	$\Delta\lambda_L$	**L**	**CL**	$\Delta\lambda_L$	**L**	**CL**	$\Delta\lambda_L$
20	889	910	21	892	925	33	885	904	19
25	879	903	24	873	899	26	883	917	34
30	873	908	35	873	907	34	902	946	44

The corresponding differences in longitudinal plasmon peak wavelength, $\Delta\lambda_L$, are shown in Table 4.3, and are presented in Figure 4.12. The largest $\Delta\lambda_L$ values are for the E2 precursor concentration at higher laser powers.

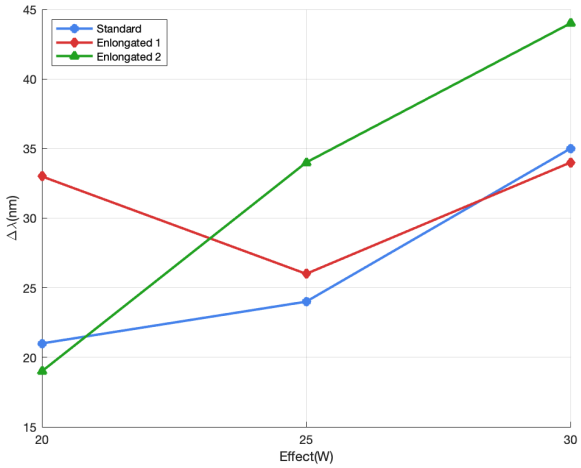

Figure 4.12: $\Delta\lambda_L$ at different laser powers (20, 25, and 30 W) for the Standard, E1, and E2 precursor concentrations.

4.1.7 Peak Width Analysis

The width of the longitudinal peak was analysed by calculating FWHM to evaluate the particle size distribution. The different conditions are summarized in Tables 4.4-4.7. ΔFWHM is calculated according to Equation 4.2:

$$\Delta FWHM = FWHM_{CL} - FWHM_L \tag{4.2}$$

where $FWHM_{CL}$ and $FWHM_L$ represent the full width at half maximum of the CL and C samples.

4.1.7.1 Standard Precursor Concentration

Table 4.4 summarizes the longitudinal plasmon peak widths for L and CL samples synthesized using the standard precursor concentration. ΔFWHM was calculated according to Equation 4.2.

Table 4.4: FWHM values for standard precursor concentrations

Power (W)	**$FWHM_L$ (nm)**	**$FWHM_{CL}$ (nm)**	**ΔFWHM (nm)**
15	103	118	15
20	120	135	15
25	111	138	27
30	117	141	24

L samples exhibited lower FWHM values than the corresponding control samples at all investigated powers. The ΔFWHM values increased from 15 nm at 15-20W to 27 nm at 25 W, followed by a slight decrease to 24 nm at 30 W. Where the largest peak width difference was observed at 25 W. Lower ΔFWHM values were observed at both lower and higher laser powers.

4.1.7.2 Effect of Synthesis Temperature

A study was done to evaluate the effects of temperature during GNR growth. Table 4.5 summarizes the FWHM obtained for samples synthesized at different temperatures. The narrowest peak was observed at 35 °C, with an FWHM value of 112 nm. When the synthesis temperature was raised to 45 °C, the peaks became broader.

Table 4.5: FWHM values for standard precursor synthesis at different temperatures

Temperature (°C)	**FWHM(nm)**
30	123
35	112
40	125
45	147

4.1.7.3 Modified Precursor Concentration (Elongated 1)

Table 4.6 summarizes the FWHM for L and CL samples synthesized using E1 precursor concentration.

Table 4.6: FWHM values for E1 precursor concentrations

Power (W)	**FWHM$_L$ (nm)**	**FWHM$_{CL}$ (nm)**	**ΔFWHM (nm)**
20	141	162	21
25	103	136	33
30	110	143	33

L samples exhibited lower FWHM values than the corresponding CL samples at all investigated laser powers. The ΔFWHM values increased from 21 nm at 20 W to 33 nm at 25 W and remained unchanged at 30 W.

4.1.7.4 Modified Precursor Concentration (Elongated 2)

Table 4.7 summarizes the FWHM for L and CL samples synthesized using E2 precursor concentration.

Table 4.7: FWHM values for E2 precursor concentrations

Power (W)	**FWHM$_L$ (nm)**	**FWHM$_{CL}$ (nm)**	**ΔFWHM (nm)**
20	122	142	20
25	112	148	36
30	142	152	10

L samples exhibited lower FWHM values than corresponding CL samples at all investigated laser powers. The ΔFWHM values increased from 20 nm at 20 W to 36 nm at 25 W, followed by a decrease to 10 nm at 30 W.

4.2 SEM Results

SEM analysis was performed to investigate the morphology, particle size, and surface characteristics of the synthesized samples under different processing conditions.

4.2.1 Particle Size and Aspect Ratio Analysis (ImageJ)

Figure 4.13 shows how ImageJ was used to threshold and manually remove isotropic nanoparticles, allowing AR determination for GNRs only.

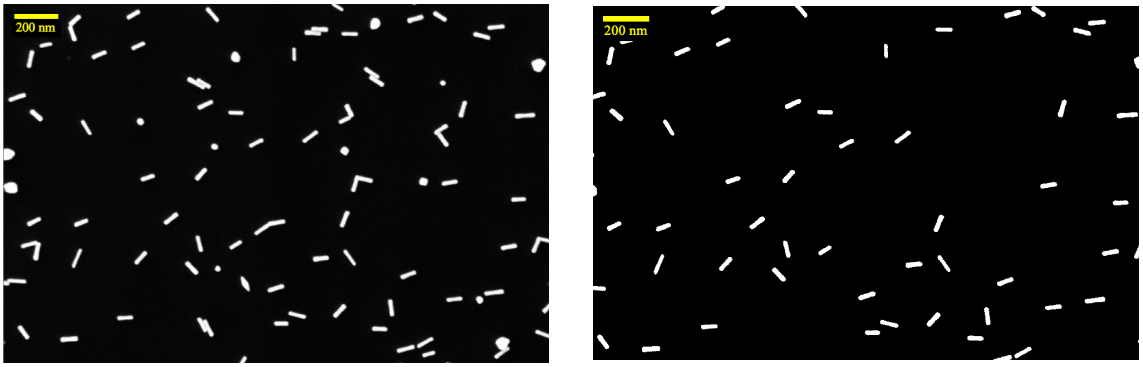

(a) **(b)**

Figure 4.13: Representative SEM image of synthesised gold nanorods (a) and corresponding binary thresholded image (b) used for AR determination in ImageJ.

Figure 4.14 illustrates a bar chart for the L samples and their respective CL. It represents the variance and mean values of the AR, providing a statistical overview of the distribution. Due to the quantity and quality of the SEM images, the sample sizes varied between 40 and 200 GNRs.

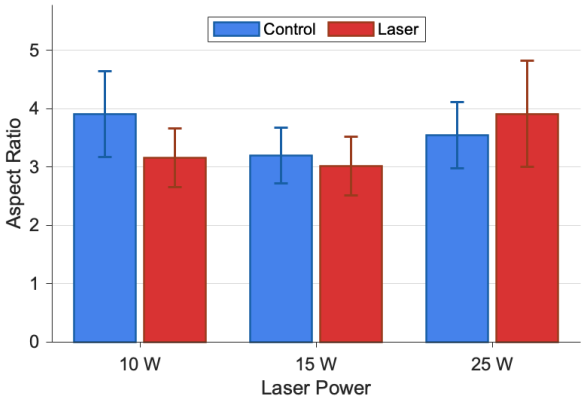

Figure 4.14: Mean AR for three groups of laser powers. 10 W: Control 3.90 ± 0.74 (N = 53); Laser 3.16 ± 0.50 (N = 140). 15 W: Control 3.20 ± 0.48 (N = 29); Laser 3.01 ± 0.51 (N = 137). 25 W: Control 3.55 ± 0.57 (N = 36); Laser 3.91 ± 0.91 (N = 34). N denotes the number of counted rods.

It should be noted that the samples used in this analysis were obtained from an early synthesis with poor temperature regulation. As shown in Figure 4.14, water temperature influences the outcome of the rods significantly. Despite this limitation, the results remain consistent with later syntheses performed under improved temperature control, as shown in figure A.3 in Appendix A.

Figure 4.15 shows representative SEM images of the 30 W CL sample (E2), where particle aggregation was observed. These aggregates contributed to higher measured aspect ratio values in the ImageJ analysis.

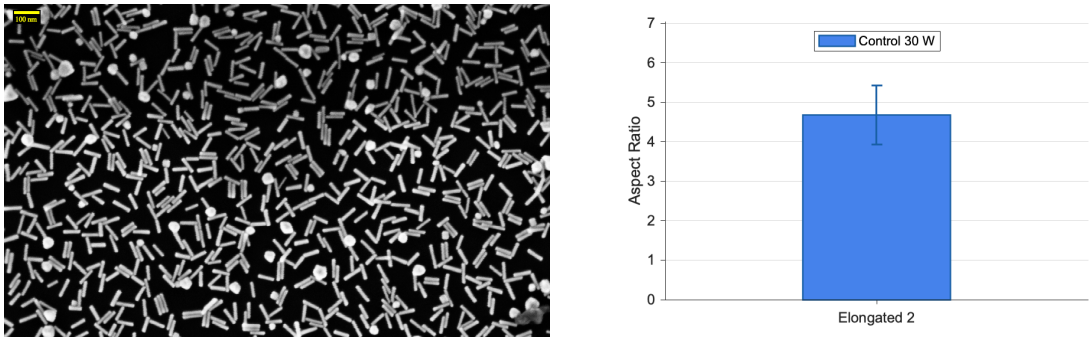

(a) **(b)**

Figure 4.15: (a) SEM images of the 30 W CL sample (E2). (b) shows AR variance of 30 W CL (E2), with a mean value of 4.67 ± 0.75.

4.2.2 Effects of Laser Irradiation

Figure 4.16 reveals morphological change when the synthesis is irradiated with NIR light, indicating the presence of spherical and irregularly shaped nanoparticles in clusters. As for the non-irradiated, it reveals a high yield of GNRs with a relatively uniform morphology.

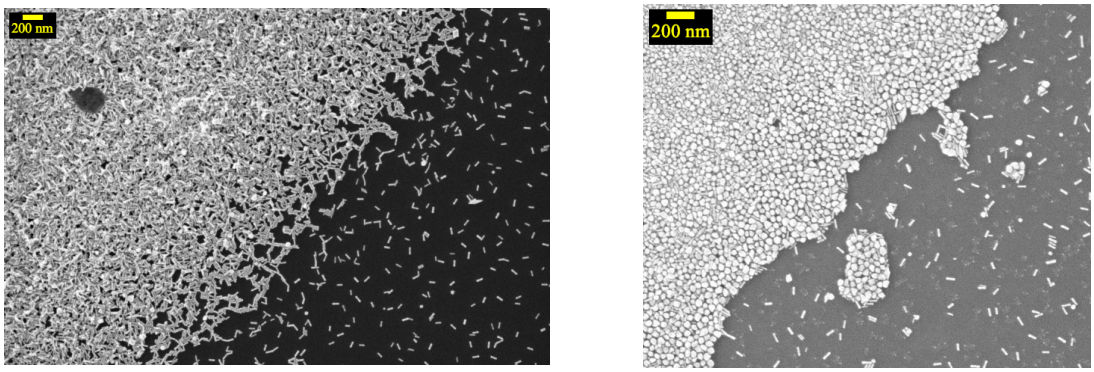

(a) **(b)**

Figure 4.16: (a) Standard CL sample at 15 W. (b) Standard L sample for 15 W.

This study demonstrates that irradiated synthesis tends to make bigger spheres. Figure 4.17 illustrates the variation of Rod-index for L and CL groups, later to be

confirmed by SEM images. The low Rod-index indicates other shapes are present in the synthesis. The L samples show slightly higher Rod-index values than the CL counterparts, except at 25 W. The highest rod purity is observed at 30 W for both conditions, suggesting that a stronger laser effect promotes greater nanorod formation. As shown in Figure 4.17, the rod index varied between the investigated laser powers, with the highest values observed for the 30 W.

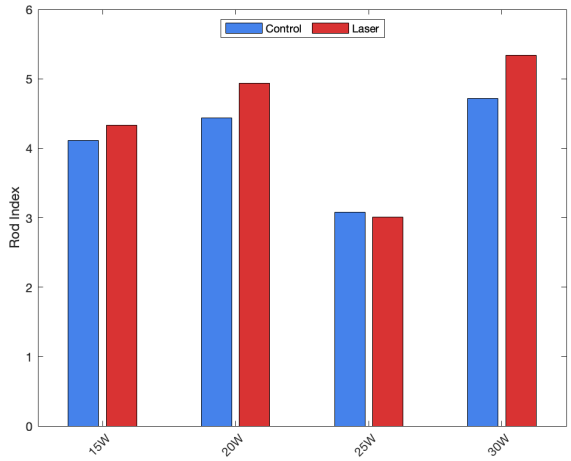

Figure 4.17: Rod Index of GRNs that were laser-irradiated at different powers.

4.2.3 Effect of Temperature on Particle Dimensions

Figure 4.18 illustrates the frequency distribution of AR across different temperatures, indicating a decrease in mean AR value as the temperature is increased (exception from 35 °C).

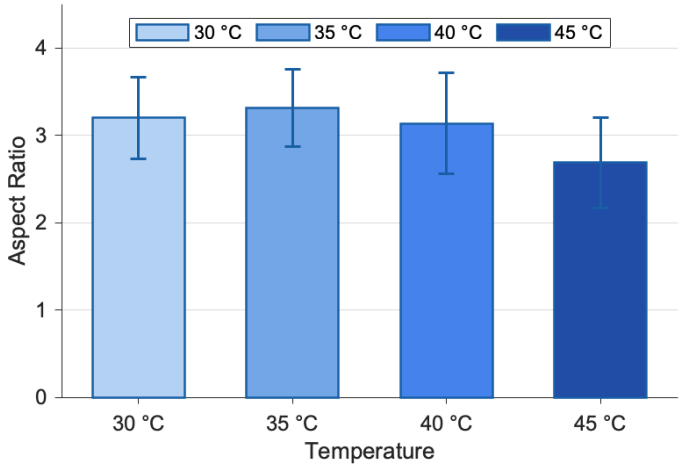

Figure 4.18: Variance of AR values for GNRs synthesised at different temperatures. 30 °C: 3.20 ± 0.47 (N = 206); 35 °C: 3.31 ± 0.44 (N = 107); 40 °C: 3.14 ± 0.58 (N = 191); 45 °C: 2.69 ± 0.51 (N = 30). N denotes the number of counted rods.

Figure 4.19 gives a relationship between synthesis temperature and rod index, with the highest rod purity at 30°C (∼4.5–4.6) and a progressive decline as the temperature increases, reaching the lowest value at 45°C (∼2.8–2.9).

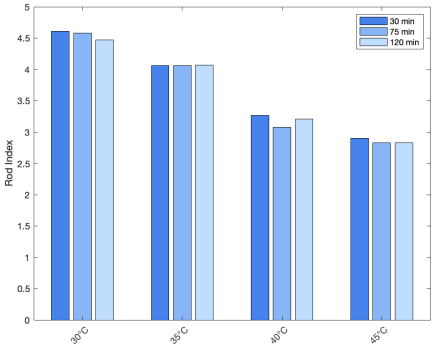

Figure 4.19: Rod index for GNRs synthesised at various temperatures.

4.2.4 Laser Effect on Precursor Concentration

SEM analysis for samples that were synthesised at different concentrations, E1 and E2, has not revealed any visual difference in morphology relative to their control groups. The particles remained rod-shaped without any noticeable misconfiguration.

All samples at different powers demonstrate very similar nanorod morphology. However, the particle density in Figure 4.20 is a direct effect of the forces present during the preparation phase.

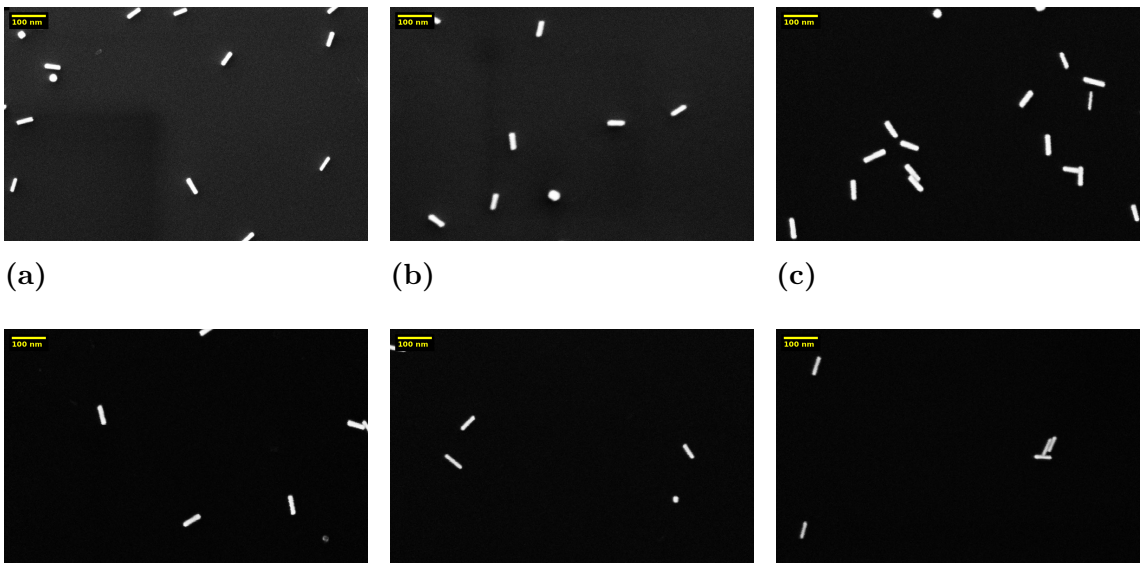

Figure 4.20: SEM images from the E2 precursor concentration across three different powers. (a, b) L and their respective CL sample at 20 W. (c, d) L and their respective CL sample at 25 W. (e, f) L and their respective CL sample at 30 W.

Table 4.8 displays the variance of AR values obtained by SEM-images, where the AR mean values of E2 CL samples indicated an increase in GNR elongation.

Table 4.8: AR values obtained from SEM analysis. AR values are reported as mean ± standard deviation, with N denoting the number of counted rods.

Sample	E1	E2
(a) L samples		
20 W	3.79 ± 0.71 ($N = 135$)	3.49 ± 0.40 ($N = 105$)
25 W	2.88 ± 0.37 ($N = 101$)	3.67 ± 0.51 ($N = 48$)
30 W	3.80 ± 0.81 ($N = 256$)	3.71 ± 0.77 ($N = 71$)
(b) CL samples		
20 W	3.54 ± 0.59 ($N = 144$)	3.55 ± 0.55 ($N = 147$)
25 W	—	3.99 ± 0.60 ($N = 62$)
30 W	—	4.26 ± 0.71 ($N = 55$)

Table 4.8 displays that all L samples with E2 concentrations exhibit shorter mean AR values compared to their corresponding CL values. Although some E1 date could not be recollected, the mean AR for L samples has a minimum at 25 W, in comparison to higher and lower laser effects.

4.2.5 Correlation Between SEM Observations and UV-Vis

Figure 4.21 presents a grouped bar chart comparing ARs of varying precursor concentration. The UV-Vis derived formula from Figure 3.1 yields higher AR values (∼4.7–5.5) compared to SEM (∼3.5–4.2) across all observations.

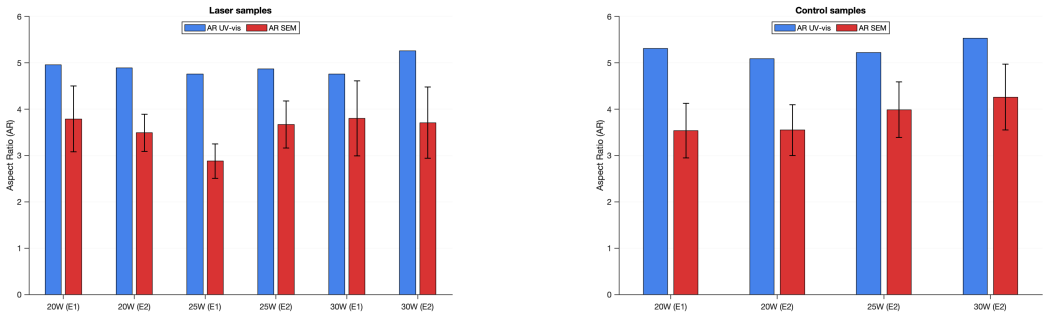

(a) **(b)**

Figure 4.21: Comparison of AR values obtained from UV-Vis spectroscopy(blue bars) and SEM analysis (red bars).(a) are the L samples, and (b) CL samples.

Figure 4.21 illustrates UV-Vis measurements consistently resulted in higher AR values compared to SEM analysis. Data collected from the 30 W CL and 25 W CL

samples with E1 concentrations could not be obtained due to contamination of the samples, being absent from the dataset.

4.3 DLS Results

DLS measurements were performed using several dilution series for both CL and L samples, with varying laser settings and precursor concentrations. Dilution series showing stable hydrodynamic diameter values were selected for future analysis.

4.3.1 Hydrodynamic Diameter

The hydrodynamic diameter (D_H) was determined using DLS for the Standard, E1, and E2 from both CL and L conditions. The mean D_H values for measurements performed at 20, 25, 30 W are presented in Figure 4.22. For each sample, the plotted values are represented by the mean ± standard deviation calculated from the selected dilution series used in the DLS analysis. The corresponding DLS measurements are presented in tables A.3-A.5, in Appendix A.

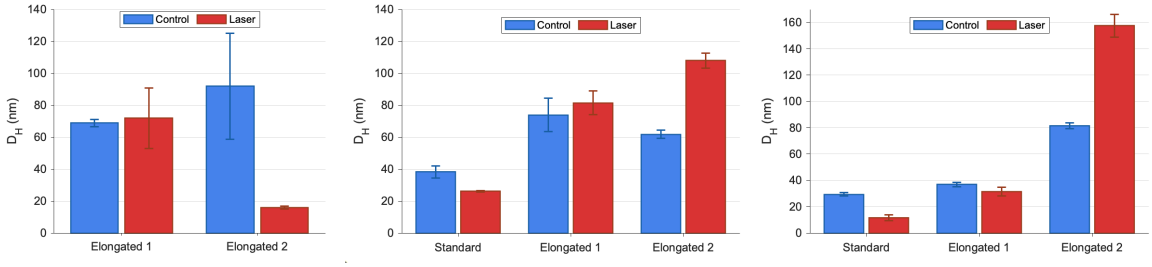

(a) **(b)** **(c)**

Figure 4.22: Mean D_H obtained from DLS measurements for standard, E1, and E2 samples. The samples are shown for CL and L conditions at laser powers of (a) 20 W, (b) 25 W, and (c) 30 W.

The values for standard precursor concentrations at 20 W in Figure 4.22a could not be obtained due to contamination.

4.3.2 Polydispersity Index

The polydispersity index (PDI) for the standard, E1, and E2 samples under CL and L conditions is shown in Figure 4.23. The plotted values represent mean ± standard deviation calculated from the selected dilution series used in the DLS analysis. The corresponding DLS measurements are presented in tables A.3-A.5, in Appendix A.

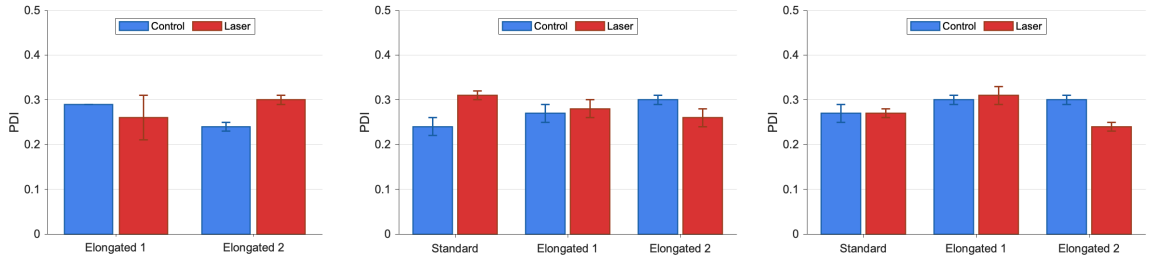

(a) **(b)** **(c)**

Figure 4.23: Mean PDI obtained from DLS measurements for Standard, E1, and E2 samples. The samples are shown for CL and L conditions at laser powers of (a) 20 W, (b) 25 W, and (c) 30 W.

The values for standard precursor concentrations at 20 W in Figure 4.23a could not be obtained due to contamination.

4.3.3 Peak Position

The peak position obtained from the DLS measurements for the standard, E1, and E2 samples under CL and L conditions is shown in Figure 4.23. The plotted values represent mean ± standard deviation calculated from the selected dilution series used in the DLS analysis. The corresponding DLS measurements are presented in tables A.3-A.5, in Appendix A.

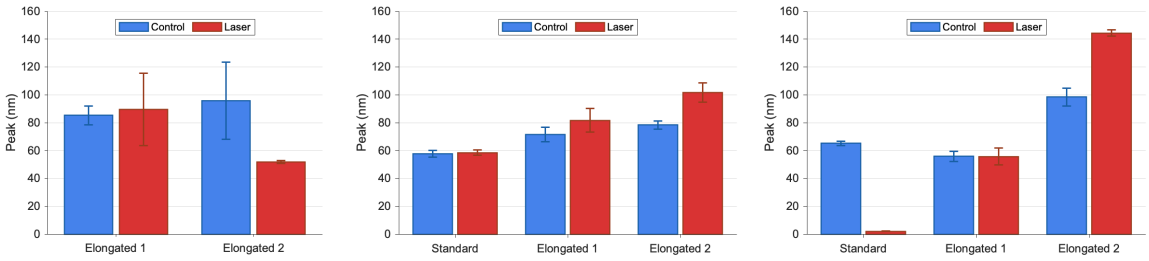

(a) **(b)** **(c)**

Figure 4.24: Mean peak position obtained from DLS measurements for standard, E1, and E2 samples. The samples are shown for CL and L conditions at laser powers of (a) 20 W, (b) 25 W, and (c) 30 W.

The values for standard precursor concentrations at 20 W in Figure 4.24a could not be obtained due to contamination.

5
Discussion

The following section discusses the observations in terms of spectral evolution, morphological changes, and colloidal stability induced by laser irradiation.

5.1 Time-Resolved Spectral Development

The results show that laser irradiation affects the temporal evolution of the synthesis process. As seen in Figure 4.4a, the L samples undergo rapid spectral changes sooner than the CL samples, after which the growth gradually slows down and starts looking like a plateau.

5.1.1 Thermal Effects During Laser Irradiation

The temperature measurements presented in Table A.2 further suggest that laser irradiation increases the reaction temperature during synthesis. For all investigated laser powers, the laser-exposed samples exhibited slightly higher temperatures than their corresponding control samples throughout the experiment. In addition, visible condensation was observed more clearly in the laser setup, as shown in Figure 4.8. This indicates enhanced evaporation within the irradiated system.

One possible explanation for the accelerated spectral evolution is therefore that laser irradiation induces localized heating of the reaction mixture. Increased temperature may enhance reaction kinetics and particle growth rates, resulting in the faster spectral development observed for the L samples in comparison to CL samples. Evaporation of water during irradiation could also increase the precursor concentration over time, which may partly explain the higher absorbance observed for the L samples.

5.1.2 Temperature-Dependent Spectral Shifts

To understand whether temperature alone could produce similar spectral changes, additional syntheses were carried out at 30 °C, 35 °C, 40 °C, and 45 °C. As shown in Figure 4.9, increasing the synthesis temperature shifted the longitudinal plasmon peak towards lower wavelengths at all investigated reaction times. A similar blue shift was also observed for the L samples when the laser power was increased.

Figure 4.10 further demonstrates that this trend remained consistent throughout the synthesis, where higher temperatures produced lower longitudinal plasmon peak

positions after 30, 75, and 120 minutes. This suggests that temperature directly influences the spectral evolution and may affect the nanoparticle growth behaviour during synthesis.

At the same time, the measured temperature differences between the L samples and their corresponding CL were relatively small; when looking at Table A.2, the difference is around 1-5°C. However, as discussed previously, laser irradiation can contribute to a larger blue shift than the shift between 30 °C and 35 °C. This suggests that elevated temperature contributes to the observed blue shift, although laser irradiation may also influence the synthesis through an additional effect apart from bulk heating alone.

5.1.3 Longitudinal Plasmon Peak Shift

The spectral differences were not limited to absorbance intensity alone. As shown in Table A.1, all L samples exhibited lower longitudinal plasmon peak positions compared to their corresponding control samples. The wavelength difference also became larger with increasing laser power, as shown in Table 4.1.

Since the longitudinal plasmon resonance is closely related to the nanoparticle AR, the observed blue shift may indicate that the L samples formed particles with lower aspect ratios. Based on Equation 2.3, this could mean that the nanorods either become shorter due to reduced longitudinal growth or wider during synthesis.

5.1.4 Elongated Nanorod Synthesis

To investigate whether nanorods with higher longitudinal plasmon peaks were affected differently by laser irradiation, additional syntheses were performed by using modified precursor concentrations to produce elongated GNRs. The resulting UV-Vis spectra are shown in the Figure 4.11, while the longitudinal plasmon peak positions and corresponding $\Delta\lambda_L$ values are presented in Table 4.3.

For all synthesis conditions, the L samples showed lower longitudinal plasmon peak positions than their corresponding control samples, similar to the standard synthesis. The difference between the laser and control samples also generally became larger with increasing laser power. This behaviour was most noticeable for the E2 synthesis, where the 30 W sample produced the largest wavelength shift of 44 nm shown in Table 4.1. Another observation is that the longitudinal plasmon peaks of the L samples remained within a relatively narrow wavelength range, even though the control samples differed more clearly from each other. The control samples reached peak positions up to 946 nm, whereas the laser-irradiated samples stayed closer to 870-910 nm. This could indicate that the laser irradiation limits the longitudinal growth of particles that would otherwise give higher AR values.

The E1 samples did not follow the same trend as clearly as the standard and the E2 synthesis. In this case, the 20 W and 30 W samples produced nearly identical

wavelength shifts. One possible explanation is that the synthesis itself was less stable under these conditions, leading to larger variation between samples.

Although the observed blue-shifts increased with laser power, the longitudinal plasmon peak position of the L samples remained relatively similar for the standard, E1, and E2 syntheses despite the larger differences observed for the CL samples. One hypothesis is that their behaviour is directly related to the wavelength of the diode laser ($\lambda \approx 808$ nm) or if the laser irradiation primarily influences the synthesis through thermal effects [20].

5.1.5 Narrowing of the Longitudinal Plasmon Peak

The FWHM analysis presented in Tables 4.4, 4.6, and 4.7 showed that the L samples consistently exhibited narrower longitudinal plasmon peaks compared to their corresponding CL samples. Since the longitudinal plasmon peak width is related to the spread in nanoparticle size and AR, this suggests that laser irradiation may promote a more uniform particle population during synthesis. The effect was observed for all investigated laser powers and precursor concentrations, indicating that the narrowing was not limited to a specific synthesis condition.

For the standard precursor synthesis shown in Table 4.4, the difference in FWHM between the L and CL samples generally increased with laser power. However, the narrowest overall longitudinal plasmon peak was observed for the 15 W L sample. A similar behaviour was observed for the elongated nanorod synthesis in Tables 4.6 and 4.7, where the largest reduction FWHM occurred at 25 W for both the standard synthesis and the E1 samples. Indicating that increasing laser power does not continuously improve the uniformity of the synthesized particles. Instead, an intermediate laser power may provide more favourable conditions for controlled nanorod growth.

The temperature-dependent synthesis experiments presented in Table 4.5 showed a similar trend. The narrowest longitudinal plasmon peak was obtained at 35 °C, while higher temperatures resulted in broader peaks again. At the same time, the measured temperature increase during laser irradiation was relatively small, typically only a few degrees above the control samples. Despite this, the L samples still exhibited noticeably narrower peaks than their CL. This suggests that temperature alone may not fully explain the observed reduction in FWHM during laser irradiation.

The E1 synthesis shown in Table 4.6 decimated some of the overall behaviour. While the FWHM reduction increased from 20 W to 25 W, no further change was seen at 30 W, however, 25 W had the smallest FWHM_L, suggesting that intermediate laser powers may provide more favourable conditions for producing a narrower longitudinal plasmon peak distribution that is connected to the AR of the nanorods.

However, the UV-Vis measurements alone are not enough to determine the ex-

act structural changes of the nanoparticles, and techniques such as SEM would be needed to confirm whether the particle morphology was altered during laser irradiation.

5.2 Morphological Analysis by SEM

The morphological analysis of SEM images using ImageJ is an approach that gives a reproducible method for AR calculations, as can be seen in Figure 4.13. But it is also biased by the inherent selection of the dispersed nanoparticles, which must be considered when interpreting the results.

The key limitation of using ImageJ is the exclusion of the aggregated parts of the sample during the threshold processing. As elongated particles exhibit stronger van der Waals interactions, GNRs with higher AR are therefore more represented in the clustered regions, as can be seen in Figure 4.20c, in Appendix A. By restricting the analysis of dispersed rods, GNR with higher AR values will therefore be underestimated, resulting in a downward bias of the mean values for AR in general. This is further supported by Figure 4.21. Consequently, SEM estimated AR values should not be understood as an absolute estimate of the true sample, but rather a relative one.

Observations of SEM-images gave a lot of clusters and bound nanoparticles to each other, as can be seen in Figure 4.15. Different morphologies could easily be seen, the images can be found in Section A.2, in Appendix A.

5.2.1 UV-Vis vs. SEM Methods and Their Limitations

As shown in Figure 4.21, UV-Vis yielded constantly higher AR values than SEM across all sample conditions. The differentiation of AR values is a reflection of the method implemented and the assumptions it relies upon.

UV-Vis formula for AR predicament was determined by El-Sayed's work, which is a relationship derived from Gans Theory [14] predicting the linear dependence of $\lambda_{\max}$ on AR. This approach is said to be well established for AR value between 2 and 5, and verified by using TEM image analysis [19]. Furthermore, UV-vis accounts for all particles in the solution, including the aggregated part. This inclusion of cluster measurements can therefore affect the spectra, increasing the AR values relative to the dispersed GNRs in SEM characterizations.

The SEM-image analysis provides a direct measurement of the dispersed GNRs, which is biased, leading to an underestimation of the true AR values. This becomes evident by looking at Figure 4.8, where 25 W control and 30 W control for E1 only yielded clusters, making it hard to obtain data points. The absence of this data limits us to comparing the UV-Vis and SEM results for these conditions.

Neither characterization methods are sources of errors, but rather reflects assumptions in UV-Vis and bias in SEM-imaging processing. Regardless of their differences, both methods showed a trend where L samples gave lower AR values than their corresponding CL group.

5.2.1.1 Effect of Precursor Concentration

Table 4.8 shows that E2 control group has an expected trend, where AR values increase with power ($3.55 \rightarrow 3.99 \rightarrow 4.26$), which is expected from the concentration changes. As for E1, it has some kind of inconsistency ($3.54 \rightarrow 2.88 \rightarrow 3.8$), which may suggest a threshold where its growth becomes isotropic. However, this bold claim must be taken with caution as the sample sizes are small, and as mentioned in the previous section, SEM results do not tell the real AR variation.

It has also been observed that the changes in AgNO3 and AA give small peak differentiations in the UV-Vis. Meaning that both concentration and irradiation are affecting the synthesis, not one alone. Raising questions about the morphological changes and polydispersity of the samples. Table 4.6 shows a ΔFWHM jumping from 21 to 33 between 20 W and 25 W. These two datasets may suggest that 25 W is the threshold at which the laser becomes dominant. This jump is also noticeable for E2 in Table 4.7, where it jumps from 20 to 36 nm between 20 W and 25 W.

Figure 4.20 shows that no morphological changes were observed for the elongation samples and their control groups. This information, together with Figure 4.11, shows that precursor concentrations tune dimensions but not shape distributions. NIR light is the one that introduces shape changes. To conclude, UV-vis reflects the AR shift and the yield, not the type of particle formation.

5.2.2 Potential Benefits of Using Transmission Electron Microscopy

The characterization limitations that were identified above should be highlighted with the need for a more direct and high resolution imagine technique. Transmission electron microscopy (TEM) would represent an improvement to future studies, as it offers several advantages over the characterization methods employed in this study.

The images provided by SEM rely on SE for topology information, TEM transmits electrons through the sample, producing a high contrast image with greater resolution [21]. Allowing for precise measurements for both length and width at the individual nanoparticle level. This would give the ability to differentiate better between different geometries and shapes that are difficult to distinguish with SEM images. TEM resolution would allow for a more accurate and unbiased determination of AR distributions, eliminating geometric assumptions associated with ellipse-fitting in ImageJ.

5.3 Dynamic Light Scattering Analysis

The following sections discuss the limitations of DLS for nanorods and the effects of laser irradiation on hydrodynamic size and stability.

5.3.1 Limitation of DLS for Anisotropic Characterization

DLS was used across multiple dilution series for all sample conditions, with selected dilutions to further analyse. While DLS is a rapid and non-destructive technique, its application for GNRs carries limitations that need to be considered when interpreting the hydrodynamic diameter and PDI values.

Figure 2.5 shows the formula that is used in DLS. Assuming that all particles are spherical, which is not compatible with anisotropic shapes, such as GNRs. The instrument can not differentiate the contribution from the diffusion along the longitudinal axis and transversal axis, it gives a hydrodynamic diameter that represents the average of all orientations [22]. This overestimates the effective size relative to the true dimensions. Furthermore, DLS is highly sensitive to aggregates due to scattering issues, and GNRs smaller than 20 nm are small enough that their scattering intensity can not be measured [23]. Causing both underestimations and overestimations, skewing both the reported hydrodynamic diameter and PDI, which causes misleading interpretations of the data, as it masks the true dispersion of GNRs.

Figure 4.23 shows the PDI values across power effects and concentrations, which appear to be consistent. However, given the sensitivity of DLS to clusters and aggregates and its inability to differentiate GNRs with different dimensions, PDI values should therefore be interpreted cautiously and not as a direct correlation to the AR distribution.

Similar to Figure 4.24, the position peak data reflect the hydrodynamic size at the dominant scattering mode, which for the GNR sample is most likely to be influenced by the presence of aggregates in the solution rather than individual rods.

Despite these limitations, DLS can provide useful information, showing trends in hydrodynamic diameter and PDI across laser-irradiated conditions and precursor concentration. This can indicate relative changes in aggregation or particle size. The DLS data in this study should therefore be complementary with other techniques, such as UV-Vis and SEM, rather than alone.

5.3.2 Effects of Laser Irradiation on Hydrodynamic Size and Colloidal Stability

DLS was used to investigate changes in hydrodynamic size and colloidal stability following laser irradiation. The measured hydrodynamic diameters (D_H) are presented in Figure 4.22, while the corresponding PDI and peak values are shown in Figures 4.23 and 4.24.

Based on the SEM and UV-Vis results presented previously, it's expected that their D_H could theoretically be expected to become smaller after laser treatment, since shorter rods or more spherical particles would be expected to have smaller D_H. Instead, the DLS results showed mixed behaviour depending on particle morphology and laser power. Several laser-irradiated elongated samples exhibited increased hydrodynamic diameters compared to their untreated controls. In contrast, some samples showed reduced D_H if laser-irradiated.

Since DLS data are intensity weighted, even a small fluctuation of larger aggregates might influence the measured D_H. One possible explanation for the increased D_H in a laser-irradiated sample is that it could have formed aggregates. However, such interpretation remains speculation since DLS alone cannot distinguish aggregation, reshaping, or changes in diffusion behaviour.

The PDI values shown in Figure 4.23 remain within a relatively narrow range for all samples, with most values between 0.2 and 0.3, indicating moderately polydisperse systems. Only minor variations were observed following the laser treatment.

The mean peak positions shown in Figure 4.24 followed trends similar to measured D_H. Several elongated laser-irradiated samples showed shifts towards larger peak positions after irradiation, which may indicate the presence of larger structures in the solution, like aggregates.

5.4 Limitations and Future Perspectives

In this study, all the experiments were performed only once. Therefore, the results obtained in our study mostly identify trends rather than exact values. Future studies could repeat the experiments multiple times to evaluate the results and determine whether similar outcomes are consistently obtained.

Further studies could investigate a wider range of laser-powered levels to better understand how irradiation influences the growth and optical properties of GNRs. Since laser irradiation also increases the solutions temperature, future experiments could include temperature -controlled reference samples to distinguish photothermal effects further from irradiation-specific effects. For example, a control setup from external heating could be used to maintain identical temperatures between irradiated and non-irradiated samples.

Additional investigation of precursor concentrations, including $AgNO_3$, AA, and seed concentration, may also provide an improved understanding of their influence on nanorod growth and AR control during laser-assisted synthesis.

More extensive SEM analysis combined with ImageJ measurements would improve the statistical evaluation of nanorod dimensions and aspect ratios. Since DLS is primarily optimized for spherical particles, the technique shows limitations when

applied to anisotropic nanorods. Future work could therefore focus on alternative characterization approaches, such as TEM, for more accurate morphological analysis.

It would also be interesting to investigate whether lasers with different wavelengths influence nanorod growth differently under identical synthesis conditions. Since this study only examines a single laser wavelength at varying power levels and precursor concentrations, future work could compare different wavelengths while maintaining the same synthesis parameters. This could provide further understanding of how wavelength-dependent interactions with the longitudinal plasmon resonance affect anisotropic nanoparticle growth.

6
Conclusion

This Master's thesis investigated seed-mediated synthesis of GNRs under the influence of NIR light to examine the growth, morphology, and optical properties of these nanorods. The experimental results allow a better understanding of each of the initial objectives.

NIR irradiation affected the synthesis of GNRs, reaching their final longitudinal peak position sooner than the CL samples. The samples longitudinal peak was consistently blue-shifted as the power of the laser increased, reaching $\Delta\lambda$ values of 44 nm at 30 W compared to the control samples. The FWHM for L samples for standard conditions was narrowest at 15 W, and for E1 it was at 25 W, indicating favourable experimental conditions for controlled nanorod growth rather than uniformity. SEM analysis then verified this trend, showing lower AR values for laser-irradiated samples and more isotropic morphologies.

NIR light was not the only factor contributing to the morphological change. Thermal images showed that irradiated samples were a few degrees warmer than the control groups. Experiments at different temperatures revealed that elevated temperatures influenced the spectral evolution towards blue-shifting, and it broadened the distribution. However, the changes observed under laser-irradiation can not be solely explained by the measured temperature difference alone, suggesting that the laser influences synthesis through more than just heating. The effect of precursor concentrations supports this idea. By increasing $AgNO_3$ and decreasing AA concentrations, the anisotropic growth was promoted in both laser-irradiated and control groups. The E2 group highest longitudinal peak shift. This may suggest that the laser interacts with the rods rather than bulk heating alone.

The three characterization methods showed different trends, which are caused by their underlying principles. UV-Vis estimated higher AR values due to the assumptions of Gans theory. SEM estimated lower AR values because it was biased towards dispersed GNRs. DLS, however, did not provide reliable validation due to its inherent limitations for anisotropic particles such as nanorods.

Overall, these findings demonstrate that NIR irradiation provides an additional handle for tuning GNRs AR and yield during seed-mediated synthesis. Future work should focus on more accurate characterization methods, such as TEM for better resolution or more SEM for more reliable data. Finally, investigating the effect of different laser wavelengths under identical conditions would provide valuable insight

into LSPR interaction in the growth process.

Bibliography

[1] Leonardo Scarabelli, Ana Sánchez-Iglesias, Jorge Pérez-Juste, and Luis M. Liz-Marzán. A "tips and tricks" practical guide to the synthesis of gold nanorods. *Journal of Physical Chemistry Letters*, 6:4270–4279, 11 2015. doi:10.1021/acs.jpclett.5b02123.

[2] Chao Zhuang, Yifan Xu, Ningsheng Xu, Jinxiu Wen, Huanjun Chen, and Shaozhi Deng. Plasmonic sensing characteristics of gold nanorods with large aspect ratios. *Sensors*, 18:3458, 10 2018. doi:10.3390/s18103458.

[3] Qida Zong, Naijun Dong, Xiaotong Yang, Guixia Ling, and Peng Zhang. Development of gold nanorods for cancer treatment. *Journal of Inorganic Biochemistry*, 220:111458, 7 2021. doi:10.1016/j.jinorgbio.2021.111458.

[4] Xin Shi, Hannah L. Perry, and James D. E. T. Wilton-Ely. Strategies for the functionalisation of gold nanorods to reduce toxicity and aid clinical translation. *Nanotheranostics*, 5:155–165, 2021. doi:10.7150/ntno.56432.

[5] Yamei Gao, Shaohu Huo, Chao Chen, Shiyu Du, Ruiyuan Xia, Jian Liu, Dandan Chen, Ziyue Diao, Xin Han, and Zhiqiang Yin. Gold nanorods as biocompatible nano-agents for the enhanced photothermal therapy in skin disorders. *Journal of biomedical research*, 39:1–17, 10 2024. doi:10.7555/JBR.38.20240119.

[6] L A Dykman and N G Khlebtsov. Gold nanoparticles in biology and medicine: recent advances and prospects. *Acta naturae*, 3:34–55, 4 2011.

[7] Prashant K. Jain, Kyeong Seok Lee, Ivan H. El-Sayed, and Mostafa A. El-Sayed. Calculated absorption and scattering properties of gold nanoparticles of different size, shape, and composition:applications in biological imaging and biomedicine. *The Journal of Physical Chemistry B*, 110:7238–7248, 4 2006. doi:10.1021/jp057170o.

[8] Pritam Khan, Grace Brennan, James Lillis, Syed AM Tofail, Ning Liu, and Christophe Silien. Characterisation and manipulation of polarisation response in plasmonic and magneto-plasmonic nanostructures and metamaterials, 8 2020. doi:10.3390/SYM12081365.

[9] Jiapeng Zheng, Xizhe Cheng, Han Zhang, Xiaopeng Bai, Ruoqi Ai, Lei Shao, and Jianfang Wang. Gold nanorods: The most versatile plasmonic nanoparticles. *Chemical Reviews*, 121:13342–13453, 11 2021. doi:10.1021/ACS.CHEMREV.1C00422.

[10] Jie Cao, Tong Sun, and Kenneth T.V. Grattan. Gold nanorod-based localized surface plasmon resonance biosensors: A review. *Sensors and Actuators B: Chemical*, 195:332–351, 5 2014. doi:10.1016/j.snb.2014.01.056.

[11] Khalisanni Khalid, Ruzaina Ishak, and Zaira Zaman Chowdhury. *UV–Vis spectroscopy in non-destructive testing*, pages 391–416. Elsevier, 2024. doi:10.1016/B978-0-323-91150-4.00021-5.

[12] Thomas G. Mayerhöfer, Susanne Pahlow, and Jürgen Popp. The bouguer-beer-lambert law: Shining light on the obscure. *ChemPhysChem*, 21:2029–2046, 9 2020. doi:10.1002/cphc.202000464.

[13] Hatice Duman, Emir Akdaşçi, Furkan Eker, Mikhael Bechelany, and Sercan Karav. Gold nanoparticles: Multifunctional properties, synthesis, and future prospects. *Nanomaterials*, 14:1805, 11 2024. doi:10.3390/nano14221805.

[14] Jorge Pérez-Juste, Isabel Pastoriza-Santos, Luis M. Liz-Marzán, and Paul Mulvaney. Gold nanorods: Synthesis, characterization and applications. *Coordination Chemistry Reviews*, 249:1870–1901, 9 2005. doi:10.1016/j.ccr.2005.01.030.

[15] Rahul Kumar, Leonardo Binetti, T. Hien Nguyen, Lourdes S. M. Alwis, Arti Agrawal, Tong Sun, and Kenneth T. V. Grattan. Determination of the aspect-ratio distribution of gold nanorods in a colloidal solution using uv-visible absorption spectroscopy. *Scientific Reports*, 9:17469, 11 2019. doi:10.1038/s41598-019-53621-4.

[16] Shunping Han and Khuloud T. Al-Jamal. Combined facile synthesis, purification, and surface functionalization approach yields monodispersed gold nanorods for drug delivery applications. *Particle & Particle Systems Characterization*, 40, 10 2023. doi:10.1002/ppsc.202300043.

[17] Jörg Stetefeld, Sean A. McKenna, and Trushar R. Patel. Dynamic light scattering: a practical guide and applications in biomedical sciences. *Biophysical Reviews*, 8:409–427, 12 2016. doi:10.1007/s12551-016-0218-6.

[18] Elizabeth R. Fischer, Bryan T. Hansen, Vinod Nair, Forrest H. Hoyt, and David W. Dorward. Scanning electron microscopy. *Current Protocols in Microbiology*, 25, 5 2012. doi:10.1002/9780471729259.mc02b02s25.

[19] Hitachi High-Technologies Corporation. Determination of the average aspect ratio of gold nanorods (gnrs) using uh4150 uv-vis-nir spectrophotometer.

[20] David Harris-Birtill, Mohan Singh, Yu Zhou, Anant Shah, Pakatip Ruenraroengsak, Maria Elena Gallina, George B. Hanna, Anthony E. G. Cass, Alexandra E. Porter, Jeffrey Bamber, and Daniel S. Elson. Gold nanorod reshaping in vitro and in vivo using a continuous wave laser. *PLOS ONE*, 12:e0185990, 10 2017. doi:10.1371/journal.pone.0185990.

[21] Manuela Malatesta. Transmission electron microscopy as a powerful tool to investigate the interaction of nanoparticles with subcellular structures. *International Journal of Molecular Sciences*, 22:12789, 11 2021. doi:10.3390/ijms222312789.

[22] Jonathan G. Mehtala and Alexander Wei. Nanometric resolution in the hydrodynamic size analysis of ligand-stabilized gold nanorods. *Langmuir*, 30:13737–13743, 11 2014. doi:10.1021/la502955h.

[23] Emilia Tomaszewska, Katarzyna Soliwoda, Kinga Kadziola, Beata Tkacz-Szczesna, Grzegorz Celichowski, Michal Cichomski, Witold Szmaja, and Jaroslaw Grobelny. Detection limits of dls and uv-vis spectroscopy in char-

acterization of polydisperse nanoparticles colloids. *Journal of Nanomaterials*, 2013, 1 2013. doi:10.1155/2013/313081.

A

Appendix A - Supplementary Characterization Data

A.1 UV-Vis Spectroscopy

This section presents additional UV-Vis data.

A.1.1 Effect of Temperature

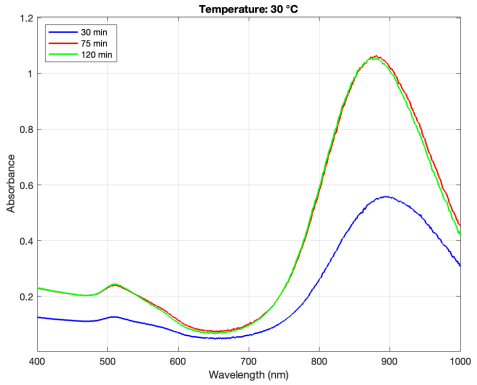

(a) 30°C

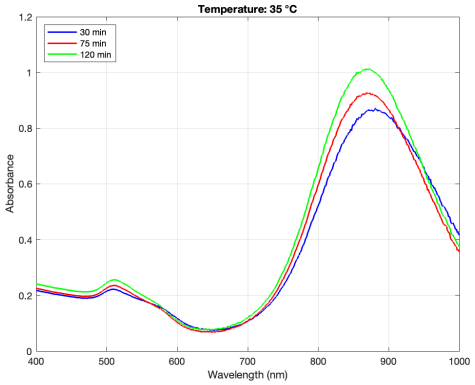

(b) 35°C

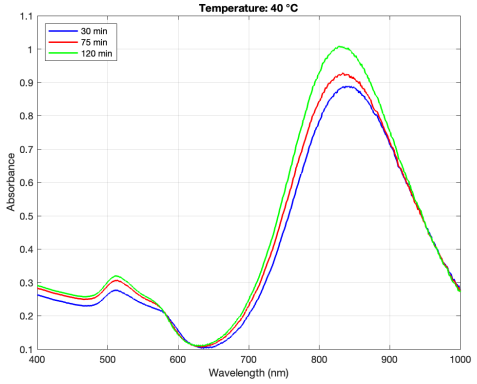

(c) 40°C

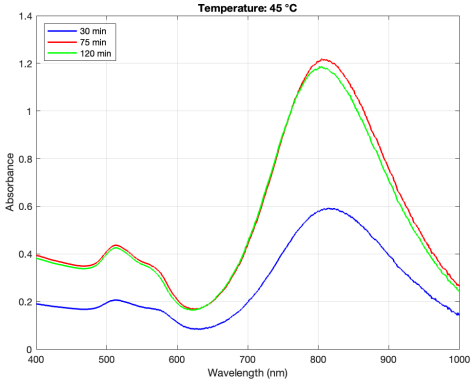

(d) 45°C

Figure A.1: Gold nanorod synthesis for varying temperatures.

A.1.2 Validation of control condition

Table A.1: Longitudinal and transverse plasmon peak positions for L, CL, and CW samples

Power (W)	**L λ_T**	**L λ_L**	**CL λ_T**	**CL λ_L**	**CW λ_T**	**CW λ_L**
15	520	877	521	887	520	889
20	521	889	521	910	520	901
25	522	879	537	903	539	907
30	520	873	520	908	520	905

A.1.3 Validation of control groups by temperature observations

Table A.2: Temperature measurements during synthesis at different laser powers and time points. L, CL, and CW temperatures were measured using a thermal camera, while L-WB and C-WB correspond to the laser and control water bath temperatures, respectively.

P (W)	**t (min)**	**L (°C)**	**CL (°C)**	**CW (°C)**	**L-WB (°C)**	**C-WB (°C)**
15	15	39.2	33.1	31.2	30.9	29.9
	30	37.0	31.8	31.1	30.4	29.6
	75	33.7	30.5	31.4	30.1	30.0
	120	32.7	32.0	31.7	30.2	30.0
20	15	34.4	33.1	32.6	30.9	30.1
	30	33.9	31.9	32.4	30.2	30.1
	75	31.4	31.1	32.3	30.2	29.7
	120	32.7	31.8	32.4	30.0	30.3
25	15	33.3	32.1	32.5	30.3	30.1
	30	35.1	31.7	31.1	30.7	29.9
	75	33.3	31.9	32.2	30.5	30.0
	120	31.5	31.4	32.8	30.0	30.0
30	15	34.8	32.1	32.6	30.9	30.1
	30	35.9	32.2	32.6	30.6	30.1
	75	35.2	31.7	32.2	30.4	30.1
	120	32.9	31.5	31.3	30.3	29.9

A.1.4 Effects of Reagent concentrations

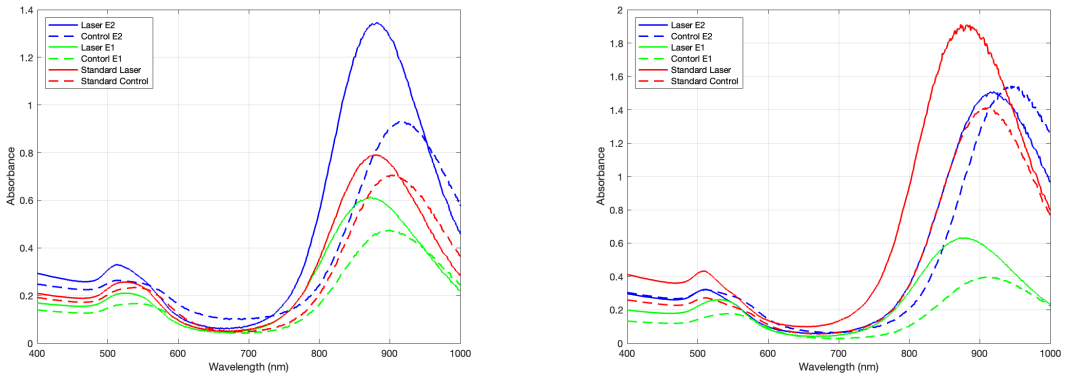

(a) 25 W **(b)** 30 W

Figure A.2: UV-Vis spectra for standard, E1, and E2 samples

A.2 SEM Images

This section presents additional SEM data, which are provided as supplementary material accompanying this thesis. SEM-images acquired in this study is available in the online repository at: `https://doi.org/10.5281/zenodo.20282677`.

A.2.1 Bar charts from SEM Images

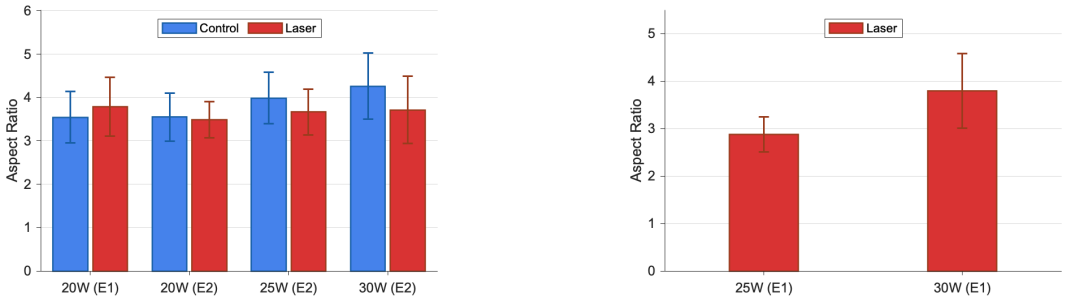

(a) **(b)**

Figure A.3: Comparison of aspect ratio (AR) values obtained from SEM analysis for (a) laser-irradiated and control samples across different laser effect and precursor conditions. (b) Samples where control data could not be obtained. Error bars represent the standard deviation.

A.3 DLS Measurments

This section presents additional DLS data.

A.3.1 DLS Measurements at 20W

Table A.3: DLS measurements for the 20 W samples. Hydrodynamic diameter (D_H), polydispersity index (PDI), and main intensity peak values are shown for the selected dilution series included in the comparative analysis.

Sample	Series	D_H (nm)	PDI	Peak (nm)
Elongated 1 Control	1:350	67.0	0.29	81.3
	1:400	68.1	0.29	81.6
	1:450	71.2	0.29	93.1
	Mean ± SD	**68.8 ± 2.2**	**0.29 ± 0.00**	**85.3 ± 6.8**
Elongated 1 Laser	1:450	53.1	0.22	62.7
	1:500	71.8	0.26	90.8
	1:550	90.8	0.31	114.6
	Mean ± SD	**71.9 ± 18.9**	**0.26 ± 0.05**	**89.4 ± 26.0**
Elongated 2 Control	1:350	54.8	0.23	66.1
	1:400	76.9	0.24	86.8
	1:450	104.6	0.25	99.7
	1:500	131.2	0.23	130.8
	Mean ± SD	**91.9 ± 33.2**	**0.24 ± 0.01**	**95.8 ± 27.2**
Elongated 2 Laser	1:300	17.4	0.29	52.0
	1:350	16.5	0.30	53.2
	1:400	16.1	0.30	51.2
	1:450	14.7	0.31	50.7
	1:500	15.9	0.29	51.0
	1:550	15.5	0.29	52.9
	Mean ± SD	**16.0 ± 0.9**	**0.30 ± 0.01**	**51.8 ± 0.9**

A.3.2 DLS Measurements at 25 W

Table A.4: DLS measurements for the 25 W samples. Hydrodynamic diameter (D_H), polydispersity index (PDI), and main intensity peak values are shown for the selected dilution series included in the comparative analysis.

Sample	Series	D_H (nm)	PDI	Peak (nm)
Standard Control	1:300	36.7	0.23	57.0
	1:350	35.7	0.26	60.6
	1:400	42.6	0.22	55.6
	Mean ± SD	**38.3 ± 3.8**	**0.24 ± 0.02**	**57.7 ± 2.5**
Standard Laser	1:350	26.8	0.30	59.8
	1:400	25.9	0.31	60.2
	1:450	25.5	0.31	58.0
	1:500	26.0	0.32	56.0
	Mean ± SD	**26.1 ± 0.5**	**0.31 ± 0.01**	**58.5 ± 1.9**
Elongated 1 Control	1:300	58.8	0.30	64.2
	1:350	75.0	0.26	75.6
	1:400	79.7	0.25	73.5
	1:450	81.9	0.27	72.8
	Mean ± SD	**73.9 ± 10.5**	**0.27 ± 0.02**	**71.5 ± 5.1**
Elongated 1 Laser	1:400	70.8	0.28	70.2
	1:450	78.2	0.28	76.9
	1:500	85.5	0.30	81.9
	1:550	84.1	0.30	89.0
	1:600	89.1	0.25	90.7
	Mean ± SD	**81.5 ± 7.3**	**0.28 ± 0.02**	**81.7 ± 8.5**
Elongated 2 Control	1:400	59.8	0.30	77.1
	1:450	61.7	0.31	77.2
	1:500	66.2	0.28	77.2
	1:550	61.8	0.30	76.2
	1:600	59.6	0.29	83.6
	Mean ± SD	**61.8 ± 2.5**	**0.30 ± 0.01**	**78.3 ± 3.0**
Elongated 2 Laser	1:450	104.1	0.24	96.1
	1:500	113.6	0.28	108.7
	1:550	103.8	0.27	94.7
	1:600	110.4	0.26	107.0
	Mean ± SD	**108.0 ± 4.7**	**0.26 ± 0.02**	**101.6 ± 7.0**

A.3.3 DLS Measurements at 30W

Table A.5: DLS measurements for the 30 W samples. Hydrodynamic diameter (D_H), polydispersity index (PDI), and main intensity peak values are shown for the selected dilution series included in the comparative analysis.

Sample	Series	D_H (nm)	PDI	Peak (nm)
Standard Control	1:350	27.6	0.29	66.1
	1:400	29.5	0.26	67.1
	1:450	29.7	0.25	63.8
	1:500	31.0	0.26	63.9
	Mean ± SD	**29.4 ± 1.4**	**0.27 ± 0.02**	**65.2 ± 1.6**
Standard Laser	1:350	12.1	0.27	1.8
	1:380	10.2	0.26	2.1
	1:400	9.4	0.27	2.1
	1:420	11.5	0.27	2.1
	1:450	14.8	0.26	1.7
	Mean ± SD	**11.6 ± 2.1**	**0.27 ± 0.01**	**2.0 ± 0.2**
Elongated 1 Control	1:300	36.7	0.30	52.7
	1:350	34.9	0.32	53.3
	1:400	38.7	0.29	56.6
	1:450	37.3	0.30	60.6
	Mean ± SD	**36.9 ± 1.6**	**0.30 ± 0.01**	**55.8 ± 3.6**
Elongated 1 Laser	1:350	30.6	0.33	47.4
	1:400	36.6	0.29	62.9
	1:450	32.1	0.30	60.4
	1:500	27.8	0.30	53.5
	1:600	29.8	0.31	54.5
	Mean ± SD	**31.4 ± 3.3**	**0.31 ± 0.02**	**55.7 ± 6.1**
Elongated 2 Control	1:350	79.2	0.28	93.3
	1:400	80.3	0.30	95.0
	1:450	82.0	0.29	97.8
	1:500	84.3	0.31	107.7
	Mean ± SD	**81.5 ± 2.2**	**0.30 ± 0.01**	**98.5 ± 6.4**
Elongated 2 Laser	1:450	150.5	0.24	141.8
	1:500	151.4	0.24	144.2
	1:550	169.2	0.24	147.6
	1:600	159.3	0.26	144.0
	Mean ± SD	**157.6 ± 8.7**	**0.24 ± 0.01**	**144.4 ± 2.4**

DEPARTMENT OF Chemistry and Chemical Engineering
CHALMERS UNIVERSITY OF TECHNOLOGY
Gothenburg, Sweden
www.chalmers.se

CHALMERS
UNIVERSITY OF TECHNOLOGY